Hydrodynamics of vertical upward and downward flow boiling in a millimetric tube

Paul Onubi Ayegba, Julien Sebilleau, Catherine Colin

Hydrodynamics of Vertical Upward and Downward Flow Boiling in a Millimetric Tube

Paul Onubi Ayegba, Julien Sebilleau, Catherine Colin

Institut de Mécanique des Fluides de Toulouse – Université de Toulouse – CNRS-INPT-UPS

Allée Camille Soula – 31400 Toulouse - France

Abstract

Upward and downward vapor-liquid vertical flows inside a vertical 6 mm sapphire tube was investigated using HFE-7000 as working fluid. The goal was to investigate the effect of flow direction and wall heating on two-phase parameters such as flow pattern, wall shear stress (τ_w), interfacial shear stress (τ_i) and interfacial wave structures. The mass flux, heat flux and vapor quality ranges were $50 \leq G \leq 400\, kg/m^2.s$, $0 \leq q \leq 3\, W/cm^2$ and $0 \leq x \leq 0.7$, respectively. Bubbly, slug, churn, annular flow patterns were observed in upward and downward flows. A falling film regime occurred in downward flow at low mass fluxes. Void fractions were higher in downward flow than in upward flow due to gravity effect, and were in good agreement with drift flux models of the literature. The wall shear stress increased with the wall heat flux due to the bubble nucleation at the wall. Following a similar approach to Kim and Mudawar (2013b), a correlation for the wall shear stress taking into account the forced convection and the bubble nucleation was derived and provided a good estimation of the experimental data within $\pm 20\%$. From image processing of the high-speed visualizations, velocities (U_w) and frequencies (F_w) of the disturbance waves in annular flow were measured. The interfacial shear stress was found to directly depend of the product $U_w \times F_w$, and a prediction of the interfacial friction factor was proposed in flow boiling for both upward and downward flows.

Keywords: flow boiling, wall shear stress, heat transfer coefficient, interfacial friction factor, wave structures, flow visualization.

1 Introduction

Two-phase flows are commonly encountered in chemical, nuclear and petroleum industries as well as other engineering applications. Recent improvements in the design and operation of thermal management systems have sort to strike a balance between improved heat dissipation and overall weight of the devices. One approach that has attracted significant research interests is the use of phase-change heat transfer. Boiling thermal management systems take advantage of the latent heat in phase change (Enoki et al., 2020; Kim and Mudawar, 2014). Boiling flow is, however, characterized by a complex interplay of hydrodynamics, mass transfer, heat transfer and interfacial phenomena. At low mass flux, boiling flows are also sensitive to gravity and the effect of gravity on such flows remains a subject of interest (Kharangate et al., 2016; Konishi and Mudawar, 2015). In horizontal or

inclined tubes, gravity tends to stratify the vapor/liquid flows or at least to induce some topological asymmetry. Even in a vertical configuration, experiments at $+1g$ (upward flow) and $-1g$ (downward flow) point out significant differences in the flow hydrodynamics and heat transfers due to the gravity (Kharangate et al., 2016; Konishi and Mudawar, 2015). A comparison of these two configurations provides useful information on the gravitational effects on two-phase flows.

Numerous studies of vertical two-phase flow patterns have been performed under adiabatic (Taitel et al. 1980, Mishima and Ishii, 1984; Bhagwat and Ghajar, 2017, 2014) and boiling (Chen et al., 2006; Enoki et al., 2020) conditions. These flow patterns include mainly bubbly, intermittent (slug and churn), falling-film (only in downward-inclined flow) and annular flows. Two-phase flow characteristics, such has bubble size and shape for bubbly flow or the liquid film thickness in annular flow have been shown to be influenced by both the flow direction (Bhagwat and Ghajar, 2012) and the gravity level (Narcy et al., 2014). Transition between the various flow patterns have also been investigated for both adiabatic (Taitel et al. 1980, Wu et al., 2017) and boiling two-phase flows. Bubbly-slug transition is due to bubble coalescence (Colin et al., 1996) and most bubbly-slug transition criteria have been based on a critical value of the void fraction (Mishima and Ishii, 1984; Usui, 1989). Studies have also shown important differences between bubbly-slug transition in fully-developed adiabatic flow and developing boiling flow (Celata and Zummo, 2009; Narcy et al., 2014). Several intermittent-annular flow transition criteria based on void fraction, Weber number of the vapor core and Froude number of the liquid have been proposed (Mishima and Ishii, 1984; Taitel et al., 1980; Usui, 1989; Wu et al., 2017). Most of the studies of flow patterns and flow pattern transition have focused on adiabatic (upward and downward) or boiling upward two-phase flow. There are very limited investigations on flow pattern and flow pattern transitions in downward flow boiling. However downward flow are also of interest for some applications including tubular co-current and counter current heat exchangers and distillation processes involving downward falling film flow.

Void fraction (α) is important for the determination of the vapor velocity ($U_v = j_v/\alpha$, j_v being the superficial vapor velocity) in bubbly/slug flows and for the estimation of the liquid film thickness in annular flows. Techniques for measuring void fraction are mainly based on fluid conductance or fluid capacitance (Canière et al., 2007; Ceccio and George, 1996; Gardenghi et al., 2020). The evolution of void fraction with superficial gas velocity or quality have been shown to be sensitive to gravity (Almabrok et al., 2016; Bhagwat and Ghajar, 2012; Narcy et al., 2014). This is due to the changes in drift velocity (U_∞) with gravitational acceleration in bubbly and slug flow regimes and the liquid film thickness in annular flow. Measurements of void fraction in downward boiling flow are limited.

Experimental measurements of wall shear stress (τ_w) in two-phase flow have been focused on adiabatic flows or on the adiabatic section of boiling flows (Dalkilic et al., 2008; Khodabandeh, 2005; Maqbool et al., 2012; Tran et al., 2000). Several correlations and models have been developed based on the compilation of extensive experimental pressure drop data (Lockhart and Martinelli, 1949; Muller-Steinhagen and Heck, 1986; Cioncolini and Thome, 2017; Kim and Mudawar, 2014). Fewer measurements of the wall shear stress have been performed on diabatic test section. It has been reported that there may be significant difference between wall shear stress in adiabatic section of a

boiling flow and in the boiling flows section itself, especially in the nucleate boiling regime (Layssac, 2018). Bubble nucleation at the heated wall in boiling flows alters the velocity profile close to the wall which in turn modifies the wall shear stress. Quantification of the effect of wall heat flux on wall shear stress is limited (Kim and Mudawar, 2013b). Most of the existing models for the wall shear stress do not account for the effect of wall heat flux. Furthermore, wall heat transfer is linked to the friction velocity ($u^* = \sqrt{\tau_w/\rho_l}$) and accurate measurement of wall shear stress in the heated tube section provides bases for the development of models for predicting wall heat transfer (Cioncolini and Thome, 2011).

The interfacial shear stress (τ_i) is of a great importance in the dynamics of annular flows. At the time of this report, the authors are not aware of any experimental data on interfacial shear stress in the heated section of boiling flows. Data reported in the literature on the measurement of interfacial shear stress concerns adiabatic flows (Asali et al., 1985; Fore et al., 2000; Fukano and Furukawa, 1998; Narcy et al., 2014). This is particularly the case with downward boiling flow. However, there is significant data on interfacial shear stress measurements in the adiabatic section of boiling flows. Models for predicting the interfacial friction factor (f_i) have been focussed on two-phase flows at very high gas Reynolds number ($Re_v \geq 30{,}000, f_v \approx 0.005$) (Belt et al., 2009; Wallis, 1969). Under such flow conditions, the interfacial friction factor is a function of the liquid film thickness (δ) alone. At lower gas Reynolds number, the turbulent gas flow is not fully developed and Fore et al. (2000) demonstrated that the interfacial friction factor was a function of both the liquid film thickness and the Reynolds number of the vapor gas core flow. They proposed modifications to the model of Wallis (1969) to account for the gas Reynolds number dependence. Interfacial shear stress strongly depends on the wave parameters such as wave amplitude, wave velocity and wave frequency. These parameters have mainly been investigated in adiabatic gas-liquid flows (Azzopardi, 1986; Barbosa et al., 2003; Dasgupta et al., 2017) for the prediction of liquid droplet entrainment. Measurement of wave parameters in flow boiling are limited especially in downward flows. Experimental data on wave parameters provides bases for developing or improving models for predicting interfacial friction factor. Models and correlations linking wave parameters to interfacial friction factor are also limited in the literature. Such models could provide a means of quantifying the interfacial friction factor from easily accessible data.

In flow boiling, numerous studies focused on the measurements and modelling of heat transfer. Review articles provide very useful correlations based on analysis of very large experimental data bases in the convective boiling regime (Cioncolini and Thome, 2011) and in the convective and nucleate boiling regimes (Kandlikar, 1990; Kim and Mudawar, 2013a).

The reviewed literature shows that there is limited data on downward flow boiling. It also shows limited data on the effect of bubble nucleation on wall and interfacial shear stresses in both upward and downward flows. This work therefore focusses on the hydrodynamics of flow boiling in the heated section of a vertical 6 mm internal diameter tube for both upward and downward flows. The paper begins with a description of the experimental facility, measurement techniques used and data

reduction methods applied. This is followed by the presentation of experimental results; flow visualization, void fraction, wall shear stress, interfacial shear stress and structure of the liquid film in annular flow. The experimental results are also compared with existing and proposed correlations.

All the data presented in this manuscript are provided as a supplementary material.

2 Experimental Setup and measurement techniques

2.1 Hydraulic loop

The experimental setup used for this work was designed for flow boiling experiments in millimetric tubes (Fig.1). The working fluid used was 1-methoxyheptafluoropropane ($C_3F_7OCH_3$) refrigerant, commonly called HFE-7000. Liquid HFE-7000 was first pumped by a gear pump (L21755 Micropump, with the DC-305A motor) and the liquid flow rate was measured using a Coriolis flow meter. The liquid was then preheated using two pre-heaters connected in series. Preheated single-phase liquid or two-phase vapor-liquid flow entered a 22 cm long vertical adiabatic section located just upstream of the test section. The adiabatic section was made of stainless steel which was insulated and this section enabled the flow to fully develop. The flow then entered the test section at pressures which can be varied from 1 to 2 bar ($34^oC < T_{sat} < 54^oC$) and a mass flux in the range of $40\ kg.m^{-2}s^{-1} < G < 400\ kg.m^{-2}s^{-1}$ can be attained in the loop. The test section consisted of a vertical transparent sapphire tube of 6 mm ID, 200 mm long and 1 mm thick, coated externally with ITO for Joule heating. The thickness of the ITO coating was 100 nm and the coated length was 180 mm. The coating was transparent allowing flow visualization with a high-speed camera at the same time as fluid heating and vaporization. Vapor quality at the outlet of the test section was determined by enthalpy balance along the test section and in general an outlet vapor quality of up to 0.9 is attainable in the loop. Fluid exiting the test section was condensed and cooled to the desired temperature at the inlet of the pump using two PID-controlled Peltier modules in the condenser. The pump inlet temperature was set to $\leq T_{sat} - 10^oC$. Table 1 provides a summary of test conditions at the inlet of the test section along with the nominal heat flux at the test section. Three experimental runs were carried out for each condition provided in Table 1. This experimental set-up allowed the determination of void fraction, vapor velocity, wall shear stress, interfacial shear stress and heat transfer coefficient in a vertical tube of 6 mm ID and 8 mm OD in upward and downward vertical flow configurations. Analysis of images obtained from high-speed visualization was also used in this work to describe the flow patterns and interfacial structures in annular flow.

Table 1. Test conditions

	Upward flow	Downward flow
$\mathbf{1.2 \leq P \leq 1.5\ bar}$	$15 \leq \Delta T_{sub} \leq 5,\ 0 \leq x_{in} \leq 0.3$	$15 \leq \Delta T_{sub} \leq 5,\ 0 \leq x_{in} \leq 0.3$
$\boldsymbol{G \approx 50\ kg/m^2s}$	$q_w = 0.5, 1.0, 1.5$ and $2.0\ W/cm^2$	$q_w = 0.5, 0.75, 1.0$ and $1.5\ W/cm^2$
$\boldsymbol{G \approx 75\ kg/m^2s}$	$q_w = 0.75, 1.0, 1.25, 1.5$ and	$q_w = 0.50, 0.75, 1.0, 1.5$ and

	2.0 W/cm^2	2.0 W/cm^2
$\boldsymbol{G \approx 100\ kg/m^2s}$	$q_w = 1.0, 1.5, 2.0, 2.5$ and 3.0 W/cm^2	$q_w = 0.75, 1.0, 1.25, 1.5$ and 2.0 W/cm^2
$\boldsymbol{G \approx 200\ kg/m^2s}$	$q_w = 1.0, 1.5, 2.0, 2.5$ and 3.0 W/cm^2	$q_w = 1.0, 1.5, 2.0, 2.5$ and 3.0 W/cm^2
$\boldsymbol{G \approx 400\ kg/m^2s}$	$q_w = 1.0, 1.5, 2.0, 2.5$ and 3.0 W/cm^2	$q_w = 1.0, 1.5, 2.0, 2.5$ and 3.0 W/cm^2

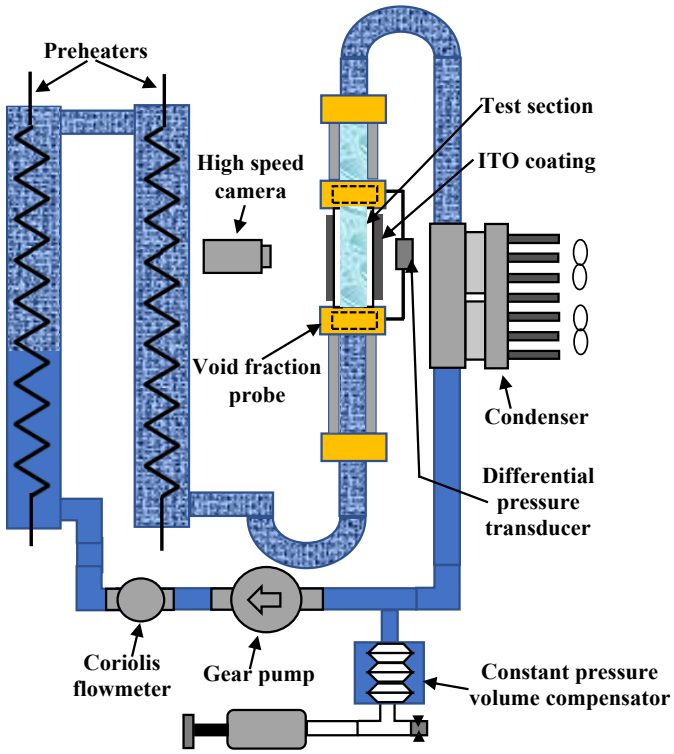

Figure 1. Experimental set-up.

2.2 Measurement techniques

Various measurement instruments were used to acquire data and these include flow meter, differential pressure transducers, absolute pressure transmitters, thermocouples, PT100 temperature probes, void fraction probes and a high-speed camera. The flow meter employs the Coriolis effect for the determination of mass flowrate with a quoted accuracy of 0.5% FS (full scale). Differential pressure measurements were done using a Validyne differential pressure (DP) transducer (model P305D, 56 cmH_2O $(FS), \delta DP = \pm 2.8\ mmH_2O$). Absolute pressure measurements were done using Keller PAA21 pressure transducers with measurement range and accuracy of $0 - 5\ bars$ and $\pm 0.25\ mbar$ respectively. These transducers provide means for measuring pressures at the different sections of the loop which are used for determining saturation temperature and for computing fluid properties. Fluid temperature measurements at various sections of the loop were done using K-type thermocouples with a stated accuracy of $\pm 0.25^oC$. Two T-type thermocouples (accuracy $\pm 0.1^oC$)

were also connected at the inlet and outlet of the sapphire tube section for measuring temperature difference across this section. Fluid temperatures were also measured using PT100 probes (accuracy $\pm 0.1^{o}C$) at the inlet of the upstream adiabatic section and at the outlet of the sapphire tube section. Pairs of outer wall temperatures were also measured at four axial distances from the inlet of the sapphire tube using PT100 probes. Additional details of each of these can be found in Narcy et al. (2014). Two capacitance probes at the inlet and outlet of the test section gave access to the void fraction (see Narcy et al., 2014). The sensitivity of the capacitance probes was $\approx 0.24\ pF$ and their measurement accuracy was estimated at $\approx 7\%$. The accuracy of the different parameters resulting from data reduction are evaluated in the Appendix. Flow visualization was carried using a high-speed camera (PCO Dimax, 2000×2000 pixels) with a spatial resolution of $\approx 12\ pix/mm$. Visualisation of the entire tube section at a frequency of 1.0 and 1.4 kHz enabled the observation of the evolution of flow pattern and wave characteristics from the inlet to outlet of the heated section.

2.3 Data reduction

2.3.1 Vapor quality and heat transfer

The fluid at the inlet of the test section was either at subcooled or saturated conditions. The inlet quality (x_{in}) was determined from the enthalpy balance across the preheater, connecting section (flexible hose) and adiabatic section (insulated stainless steel) upstream of the test section. The enthalpy balance between the inlet of the preheater and the inlet of the test section is given by Eq. 1.

$$\frac{P_{ph\_eff}}{(\pi D^2/4)} = G(1-x_{in})Cp_l T_{in} + Gx_{in}h_v - GCp_l T_{in,ph} \tag{1}$$

where T_{in} and x_{in} are the temperature and the quality at the inlet of the test section, $T_{in,ph}$ is the temperature at the inlet of the preheater, P_{ph_eff} is the preheater power after correction for heat losses, which is the effective power transmitted to the fluid (see Narcy et al., 2014). G is the total mass flux, h_v is the enthalpy of the vapor and Cp_l is the specific heat capacity of the liquid. For saturated conditions at the inlet of the test section; $Cp_l T_{in} = h_{l,sat}$, $h_v = h_{v,sat}$ and $h_{v,sat} - h_{l,sat} = h_{lv}$, $h_{l,sat}$ and $h_{v,sat}$ being the enthalpy of liquid and vapor at saturation:

$$x_{in} = \frac{4P_{ph\_eff} - GCp_l \pi D^2 (T_{in} - T_{in,ph})}{G\pi D^2 h_{lv}} \tag{2}$$

The quality (x_z) at an axial position (z) in the test section ($z = 0$ at the entrance) was obtained from the enthalpy balance between the inlet of the test section and the position z.

$$x_z = x_{in} + \frac{\left[\frac{4q_{eff} \times z}{GD} - Cp_l(T_z - T_{in})\right]}{h_{lv} + Cp_l(T_{sat} - T_z)} \tag{3}$$

At subcooled inlet conditions, $x_{in} = 0$ and at saturated inlet conditions $T_z = T_{in} = T_{sat}$, $Cp_l(T_z - T_{in}) = 0$, $Cp_l(T_{sat} - T_z) = 0$. For subcooled inlet conditions the temperature evolution between the

inlet and outlet of the sapphire tube section is assumed to be linear. The effective wall heat flux (q_{eff}) was obtained from the difference in applied heat flux (q) and estimated heat loss in the test section (see Narcy et al., 2014).

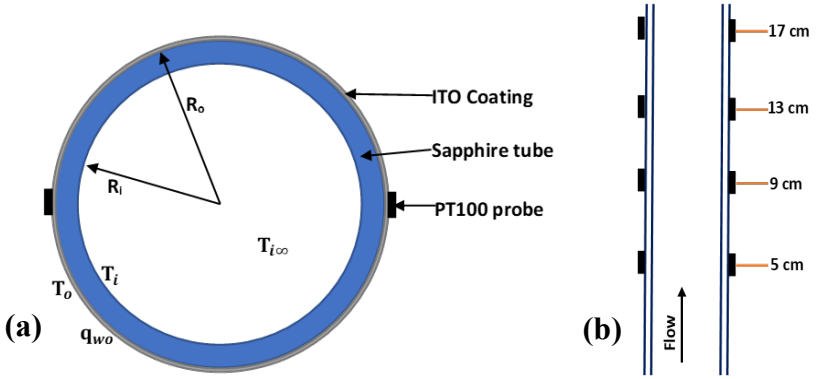

Figure 2: a. illustration of the heated tube cross section, b. illustration of axial locations of PT100 probes for wall temperature measurements

Calculation of inner wall heat transfer coefficient (h_i) was done at four (4) axial locations along the heated tube section. Schematic drawing of the tube cross section is shown in Fig. 2a and a schematic drawing showing the 4 locations where h_i was calculated is shown in Fig. 2b. The heat transfer coefficient at the inner wall can be obtained from an energy balance between the fluid and the inner wall as follows;

$$h_i = \frac{q_{eff}}{T_{ow} - T_{i\infty} - \ln\left(\frac{R_o}{R_i}\right)\frac{R_o}{k} q_{eff}} \tag{4}$$

where k is the thermal conductivity of sapphire tube, R_o and R_i are the outer and inner tube radii of the sapphire tube, T_{ow} and $T_{i\infty}$ are the outer wall temperature and the liquid bulk temperature.

Single-phase measurements at moderate wall heat flux were carried out to provide validation for the measurement technique. The measured single-phase Nusselt number (Nu) was compared to Gnielinski's correlation (1976). After correction with Al-Arabi's correlation (1982) for entrance effect and correcting for heat loss, most of the experimental Nusselt numbers at various axial locations were within $\pm 15\%$ of Gnielinski's correlation (see Appendix, Figure A1). This provides validation of the experimental technique.

2.3.2 Wall and interfacial frictions

The wall shear stress was obtained from the momentum balance equation of the mixture (Eq. 5).

$$\frac{dP}{dz} = -\frac{2}{R}\tau_w - \rho_m g \sin\theta - G^2 \frac{d}{dz}\left[\frac{(1-x)^2}{\rho_l(1-\alpha)} + \frac{x^2}{\rho_v \alpha}\right] \tag{5}$$

where $P, \tau_w, g, \alpha, x, \theta, \rho_v$ and ρ_l are the pressure, wall shear stress, acceleration due to gravity, void fraction, vapor quality, the tube inclination to the horizontal, vapor density and liquid density,

respectively. $\theta = 90^o$ in upward flow and -90^o in downward flow and mixture density is given by $\rho_m = \rho_l(1-\alpha) + \rho_v\alpha$. The first, second and third terms of the RHS of Eq. 5 are the frictional, gravitational and acceleration pressure gradients, respectively. In the current work, the acceleration term was generally non-negligible for non-adiabatic measurements and zero for adiabatic flow measurements. This term is calculated from the measurements of the void fractions and qualities at the inlet and outlet of the test section. The measured void fraction at the outlet of the tube was used to obtain a relationship between void fraction and vapor quality. The local void fraction ($\alpha(z)$) at various axial locations along the test section was determined from this relationship. The gravitational pressure drop in Eq. 5 was obtained by numerical integration of $(\rho_l(1-\alpha) + \rho_v\alpha)g\sin\theta$ along the length of the test section with fluid properties assumed constant.

Differential pressure measurements were carried out for single-phase flows for the purpose of validating the measurement techniques. The experimental single-phase wall friction factor was obtained using;

$$f_w = -\frac{dP}{dz}\frac{D\rho_l}{2G^2} \tag{6}$$

and was in good agreement with the Blasius correlation for turbulent flows ($f_w = 0.0792Re^{-0.25}$) within $\pm 10\%$ (see Appendix, Figure A1).

The interfacial shear stress (τ_i) was obtained from the momentum balance of the vapor phase (Eq. 7) using measured pressure drop and void fraction. Eq. 7 is written with the assumption of negligible liquid entrainment in the gas core. In the current work, the difference introduced by this assumption was always less than 2% (Narcy et al., 2014). The interfacial friction factor (f_i) was obtained from Eq. 8 and it is often scaled by the friction factor of the vapor core turbulent flow above a smooth interface given Eq. 9.

$$\alpha\frac{dp}{dz} = -\rho_v\alpha g\sin\theta - G^2\frac{d}{dz}\left[\frac{x^2}{\rho_v\alpha}\right] - \frac{4\sqrt{\alpha}\tau_i}{D} \tag{7}$$

$$f_i = \frac{2\tau_i}{\rho_v(U_v - U_l)^2} \tag{8}$$

$$f_v = 0.0792Re_v^{-0.25} \qquad \left(Re_v = \frac{U_vD}{\nu_v}\right) \tag{9}$$

3 Results and discussion

3.1 Flow visualization and pattern maps

Flow visualizations were carried out at various two-phase flow conditions ranging from subcooled to saturated boiling for both upward and downward flows (Fig. 3). The observed flow patterns for upward flow were categorized into bubbly, intermittent (slug, churn and other transitions flows) and annular flow regimes for $50 \le G \le 400\ kg/m^2s$. The observed flow patterns in downward flow were categorized into bubbly, intermittent, falling-film and annular flow regimes.

Bubbly flow was observed for subcooled inlet conditions. The bubble diameter and the aspect ratio (mean radial to mean axial diameter) of the bubbles were significantly larger in downward flow particularly at $G \leq 200\, kg/m^2 s$ (Fig. 3a and 3e). The slower bubble velocity in downward flow led to a longer residence time and a higher rate of coalescence. These differences, between upward and downward flow, become less obvious at higher mass flux where mixture velocity become dominant in comparison with the relative velocity (Fig. 3b and 3f). Bubbly flow regime was observed for all mass fluxes in upward flow but was only observed at $G \geq 200\, kg/m^2 s$ in downward flow. For $G = 200\, kg/m^2 s$, the liquid velocity (G/ρ_l) at the entrance of the test section is of order of magnitude of the bubble drift velocity (U_∞) which is around $0.15\ m/s$.

Fig. 3c and 3g show slug flow regime in upward and downward flow respectively. The main difference between slug flow in upward and downward flows is the shape of the bubbles. The cap of the Taylor bubbles in upward flow was sharper with a smaller curvature radius of the bubble nose relative to downward flow. In downward flow, the bubble nose is relatively flat (or distorted), with a larger radius of curvature and a thinner liquid film around the bubble. This is due to the longer mean residence time of the bubble in the heated tube section in downward flow, which led to a higher evaporation of the liquid film. The observations are consistent with that of Bhagwat and Ghajar (2017). At $G = 100\, kg/m^2 s$, stagnating or oscillating Taylor bubbles were observed in downward flow (Fig. 3h).

Falling-film regime was observed for $G \leq 200\, kg/m^2 s$ and was characterized by low liquid and low/moderate vapor velocities with the vapor core surrounded by a falling liquid film along the wall (Fig. 3i-j). The liquid film was characterized by ripples and the interface was relatively smooth (no roll waves). At heat fluxes $q \geq 1.5\ W/cm^2$, nucleate boiling was observed in the liquid film (Fig. 3j). At saturated conditions in both upward and downward flows, annular flow regime was observed (Fig. 3c and k). The annular flow regime was characterized by high velocity vapor core and liquid film flowing along the wall. Roll waves were observed in the annular flow and at high vapor qualities, interfacial stresses induced breakup of interfacial waves resulting in liquid droplet entrainment in the vapor core. The same flow patterns were observed in adiabatic two-phase flow (Bhagwat and Ghajar, 2017) except for the effect of bubble nucleation at the wall which is specific to boiling flows. Observed flow patterns in upward flow are also consistent with the report of Narcy et al. (2014). Some flow visualizations are showed in the supplementary material.

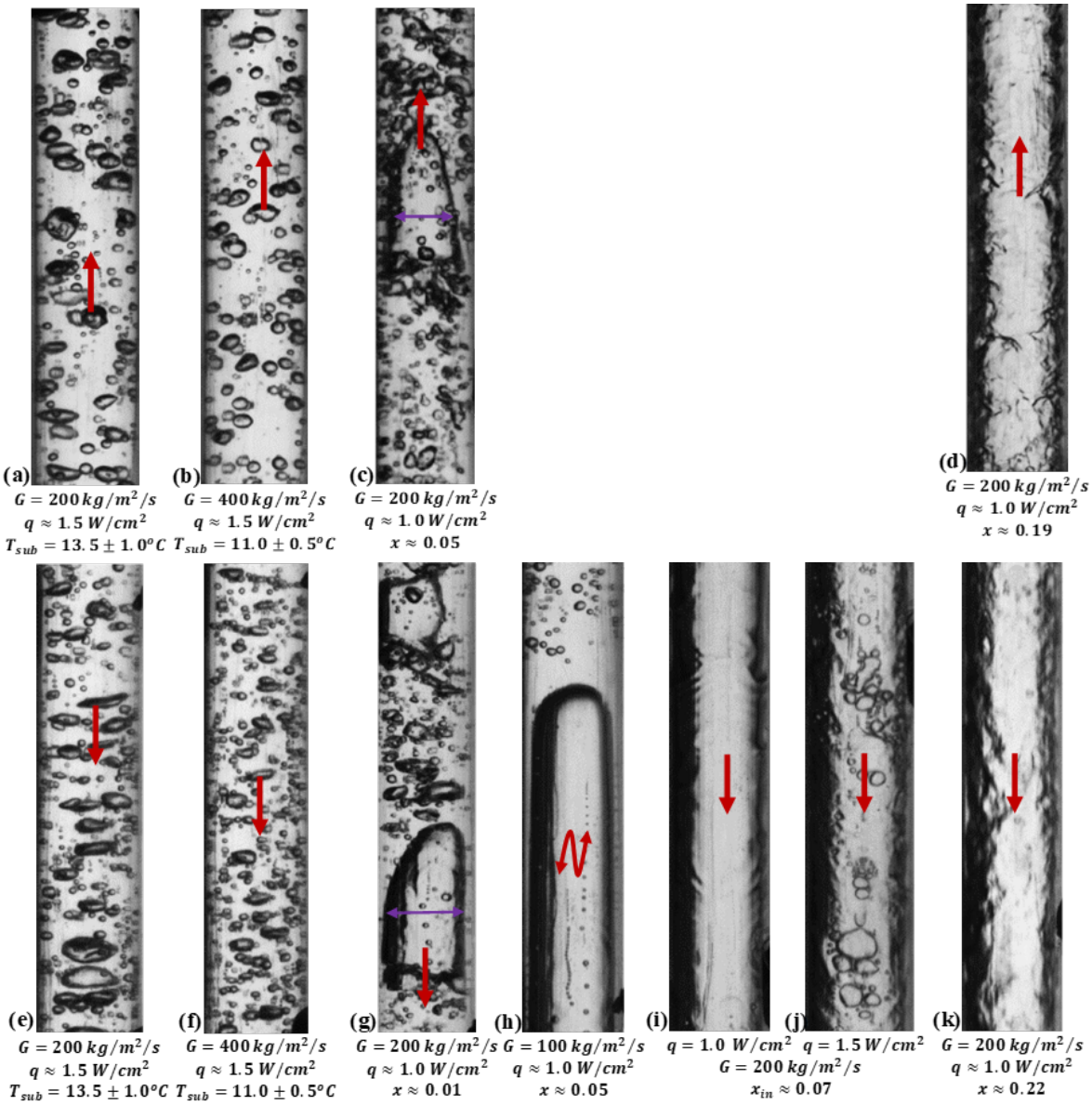

Figure 3. Flow visualization in upward and downward flows: a-b. upward bubbly flow, c. upward intermittent flow, d. upward annular flow, e-f. downward bubbly flow, g-h. downward intermittent flow, i-j. downward falling film flow and k. downward annular flow. Red arrows indicate the direction of vapor flow.

The observed flow patterns were presented in flow pattern maps in terms of liquid and vapor superficial velocities (j_l, j_v) for both upward (Fig. 4a) and downward (Fig. 4b) flows. Bubbly to intermittent flow regime transition occurred at higher void fraction in downward flow relative to upward flow. Furthermore, flow patterns in upward and downward flows become similar at significantly high flow rate ($G \geq 400\,kg/m^2s$).

In upward flow, bubbly to intermittent flow regime transition occurred for measured values of the void fraction of about 0.65 ($0.64 \leq \alpha_C \leq 0.67$). This value of critical void fraction at bubbly-intermittent flow transition is in agreement with other flow boiling experiments in upward flow where

α_C of about 0.7 was reported (Celata and Zummo, 2009; Narcy et al., 2014). Applying $\alpha_C = 0.65$ in the drift flux models of Ishii (1977) (see Mishima and Ishii (1984)) and Rouhani and Axelsson (1970), gave bubbly-intermittent flow transition boundaries shown in Fig. 4a as dotted line and solid line respectively. These drift flux models are given in Table 1 and x_C is given by Eq. 10. The model of Rouhani and Axelsson (1970) gave a reasonable prediction of the bubbly-intermittent flow transition boundary particularly at lower mass fluxes.

$$x_c = \frac{\frac{G}{\rho_l}+\frac{U_\infty}{C_0}}{\frac{G(1-C_0\alpha_c)}{\rho_v C_0 \alpha_c}+\frac{G}{\rho_l}} \tag{10}$$

In downward flow, co-current bubbly and slug flows were observed for $G \geq 200\, kg/m^2 s$ and bubbly-slug transition occurred at void fraction of ≈ 0.75. A few modelling studies have been carried out on the criteria for bubbly-slug transition in adiabatic gas-liquid downward flows (Bhagwat and Ghajar, 2015; Martin, 1976; Usui, 1989). Others proposed transition boundaries based on flow visualizations (Almabrok et al., 2016; Bhagwat and Ghajar, 2017). Usui (1989) proposed a criterion for bubbly-slug transition using the drift flux model (Eq. 11) approach with $\alpha_C = 0.175$, $C_0 = 1.2$ and u_∞ given by Eq. 12. The proposed transition boundary falls outside of the plot range of Fig. 4b. The reason for this is the significantly lower mean value of α_C used in that work. With a value of $\alpha_C = 0.75$ (current work), and same values of C_0 and U_∞ as Usui (1989), the drift flux model gave a good estimation of the bubbly-slug transition (Fig. 4b).

$$\alpha = \frac{j_v}{C_0(j_v+j_l)+u_\infty} \qquad \text{(Drift flux model)} \tag{11}$$

$$U_\infty = -1.53\left[\frac{\sigma.g.(\rho_l-\rho_v)}{\rho_l^2}\right]^{1/4} \tag{12}$$

With an increase in mass flux ($50 \rightarrow 400\ kg/m^2 s$), intermittent to annular flow regime transition was observed at slightly higher void fraction ($0.78 \rightarrow 0.84$) in upward flow. Mishima and Ishii (1984) proposed criteria for slug-churn flow regime transition (Eq. 13). Their proposed slug-churn transition boundary coincided with their proposed slug-annular transition boundary at higher mass flux. Their proposed slug-churn transition criteria gave a good prediction of our observed intermittent-annular flow transition except at the highest mass flux.

$$\alpha \geq 1 - 0.813\left\{\frac{(C_0-1)j+0.35\sqrt{\frac{(\rho_l-\rho_v)gD}{\rho_l}}}{j+0.75\sqrt{\frac{(\rho_l-\rho_v)gD}{\rho_l}}\left[\frac{(\rho_l-\rho_v)gD^3}{\rho_l v_l^2}\right]^{1/18}}\right\}^{0.75} \qquad \text{(Mishima and Ishii, 1984)} \tag{13}$$

In downward flow, slug-falling film ($G \leq 200\, kg/m^2 s$), slug-annular ($G = 400\, kg/m^2 s$) and falling film-annular ($G \leq 200\, kg/m^2 s$) flow regime transitions were observed. In a number of downward flow studies, slug-falling film regime transition is defined by a region of constant liquid

superficial velocity (Almabrok et al., 2016; Bhagwat and Ghajar, 2017; Usui, 1989). A criterion for slug-falling film regime transition was proposed by Usui (1989) (Eq. 14). The proposed transition boundary slightly over-predicts the observed transition boundary in the current work. However, substituting a value 0.8 (in place of 0.92) for K_1 in Eq. 14 provided a good estimation of the observed slug-falling film regime transition (Fig. 4b). Usui (1989) also proposed a criterion for transition from falling film/slug flow to annular flow (Eq. 15). The proposed model over-predicts and under-predicts the transition boundary in the current work at low and high mass fluxes respectively (Fig. 4b – dashed line).

$$Fr_l = \left(K_1 - \frac{K_2}{Eo}\right)^{23/18} \qquad \text{(Usui, 1989)} \qquad (14)$$

where $K_1 = 0.92$, $K_2 = 7$, $Fr_l = \frac{j_l}{\sqrt{gD(\rho_l - \rho_v)/\rho_l}}$ and $Eo = gD^2\,(\rho_l - \rho_v)/\sigma$.

$$Fr_l = 2.5(j_v/j_l)^{-2/3} \qquad \text{(Usui, 1989)} \qquad (15)$$

Overall, the accuracy of prediction of flow pattern and transition in the heated section of boiling flows appears to depend on the accuracy of measurement of the local void fraction at any axial location. For short-length millimetric tubes (as with the current work), the void fractions corresponding to the various transition boundaries were generally higher than the corresponding void fraction at transition for fully developed adiabatic gas-liquid flows.

(a)

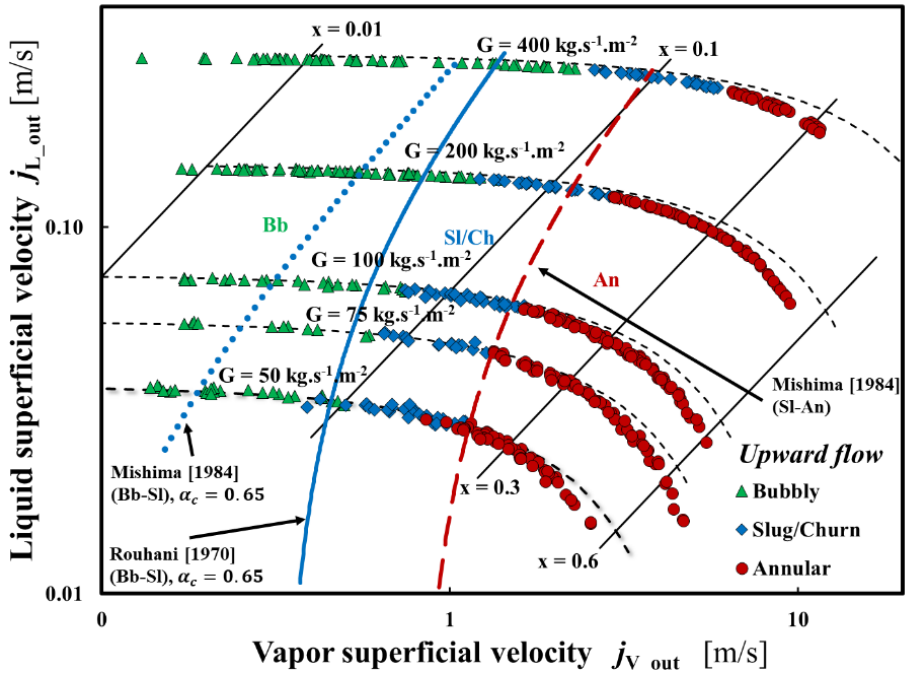

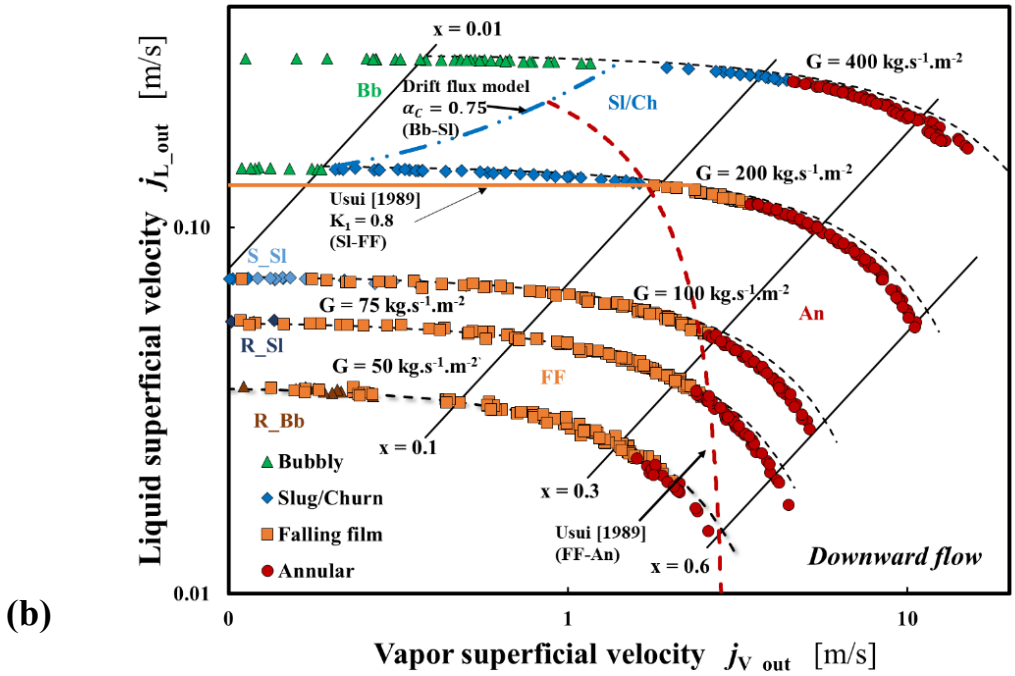

Figure 4. Flow pattern maps for a. upward flow, b. downward flow. Bb (bubbly flow), Sl (slug flow), Ch (churn flow), An (annular flow), FF (falling film flow), S_Sl (stagnant or oscillating slug flow), R_Sl (reverse slug flow), R_Bb (reverse Bb).

3.2 Void fraction and liquid film thickness

Results of measured void fraction in upward and downward flows are presented on plots of void fraction versus vapor quality. Fig. 5a shows measured void fraction versus vapor quality at the outlet of the heated tube section in upward flow. The measured void fraction increased with mass flux for $x \leq 0.3$ and this trend is in agreement with some commonly used void fraction models (Ishii, 1977; Rouhani and Axelsson, 1970; Zuber et al., 1967). The measured void fractions were also in agreement with recent void fraction measurement of Gomyo and Asano (2016) obtained inside a tube of $4\ mm\ ID$ with vapor-liquid FC-72 as working fluid (Fig. 5d-f). Two common approaches are generally used in void fraction modelling: drift flux approach (Bhagwat and Ghajar, 2014; Rouhani and Axelsson, 1970; Woldesemayat and Ghajar, 2007; Zuber et al., 1967) and separated flow approach (Lockhart and Martinelli, 1949). A review of various models for predicting the void fraction of flows in various orientations at earth gravity conditions can be found in (Bhagwat and Ghajar, 2014, 2012). Selected correlations are provided in Table 2. The model of Zuber et al. (1967) provided a good prediction of the experimental data in the range of void fraction $0.6 \leq \alpha \leq 1.0$ corresponding to intermittent and annular flow regimes while the models of Rouhani and Axelsson (1970) and Ishii (1977) gave good predictions of the experimental data in the range of void fraction $0.1 \leq \alpha < 0.6$ corresponding to bubbly and intermittent flow regimes (Fig. 5a). The model of Woldesemayat and Ghajar (2007) gave a good prediction of the measured void fraction in the intermittent and annular flow regimes. The void fraction correlation of Cioncolini and Thome (2012) provided a good estimation of the experimental data for $x \geq 0.3$. This correlation gave poor prediction at lower

quality because the model was developed for annular two-phase flows. Table 3 provides a summary of mean absolute error for selected void fraction models.

Table 2. Selected void fraction correlations.

Author	Correlation for drift velocity or void fraction
(Bhagwat and Ghajar, 2014)	$U_\infty = (0.35\sin\theta + 0.45\cos\theta)\sqrt{\frac{gD(\rho_l-\rho_v)}{\rho_l}}(1-\alpha)^{0.5}C_2C_3C_4$ where θ is measured from horizontal and expressions for determining $C_{o,1}$, C_2, C_3, and C_4 can be found in (Bhagwat and Ghajar, 2014) $C_0 = \frac{1-(\rho_v/\rho_l)^2}{1+(Re_{2\emptyset}/1000)^2} + \frac{1+C_{o,1}}{1+(1000/Re_{2\emptyset})^2}$
(Ishii, 1977)	$\begin{cases} U_\infty = \sqrt{2}\left[\frac{\sigma g(\rho_l-\rho_v)}{\rho_l^2}\right]^{0.25}(1-\alpha)^{1.75} & Bubbly\ flow \\ U_\infty = \sqrt{2}\left[\frac{\sigma g(\rho_l-\rho_v)}{\rho_l^2}\right]^{0.25} & Churn\ flow \end{cases}$ $C_0 = 1.2 - 0.2\sqrt{\rho_v/\rho_l}$
(Rouhani and Axelsson, 1970)	$U_\infty = \pm 1.18\left[g\sigma\left(\frac{\rho_l-\rho_v}{\rho_l^2}\right)\right]^{0.25}$ $C_0 = \begin{cases} 1+0.2.(1-x).(gD\,\rho_l^2/G^2)^{0.25} & for\ \alpha \le 0.25 \\ 1+0.2(1-x) & for\ \alpha > 0.25 \end{cases}$
(Zuber et al., 1967)	$U_\infty = 23\sqrt{\frac{\mu_l G(1-x)}{\rho_l\rho_v D}}, \quad C_0 = 1.0$
(Woldesemayat and Ghajar, 2007)	$\alpha = \frac{j_v}{j_v\left[1+\left(\frac{j_l}{j_v}\right)\left(\frac{\rho_v}{\rho_l}\right)^{0.1}\right]+2.9\left[\frac{gd\sigma(1-\cos\theta)(\rho_l-\rho_v)}{{\rho_l}^2}\right]^{0.25}(1.22+1.22\sin\theta)^{\frac{Patm}{P}}}$
(Cioncolini and Thome, 2012)	$\alpha = \frac{hx^n}{1+(h-1)x^n}$ where $\begin{cases} h = -2.129 + 3.129\left(\frac{\rho_v}{\rho_l}\right)^{-0.2186} \\ n = 0.3487 + 0.6513\left(\frac{\rho_v}{\rho_l}\right)^{0.5150} \end{cases}$

In downward flow, high values of the void fraction (> 0.8) were recorded at low vapor quality for $G \le 100\ kg/m^2s$, which corresponds to falling film regime and the disappearance of the bubbly co-current flow regime (Fig. 5b). In contrast to upward flow, measured void fraction decreased with increase in mass flux or liquid superficial velocity especially in the bubbly and intermittent flow regimes. This is associated with the decrease in residence time of the vapor with increase in mass flux. The general trend of measured void fraction and its mass flux dependence are consistent with other investigations for adiabatic gas-liquid downward flows (Almabrok et al., 2016; Bhagwat and Ghajar, 2012). A common approach to void fraction modelling in downward flows is the drift flux model approach with a negative drift velocity (Bhagwat and Ghajar, 2012; Usui and Sato, 1989). Fig. 5b show comparison of measured void fraction with the model of Rouhani and Axelsson (1970). The

model provided a good prediction of measured void fraction for $G \leq 200\ kg/m^2s$ both in magnitude and trend.

Table 3. Mean Absolute Error for various void fraction correlations.

Model/Correlation ($\boldsymbol{G = 50 - 400\ kg/m^2s}$)	Upward flow (MAE %)	Downward flow (MAE %)
Rouhani and Axelsson (1970) (IN/AN)	15.7	2.8
Ishii (1977) (IN)	27.0	
Bhagwat and Ghajar (2014) (IN/AN)	9.6	5.2
Woldesemayat and Ghajar (2007) (IN/AN)	6.8	
Zuber et al. (1967) (AN)	2.5	
Cioncolini and Thome (2012) (AN)	5.4	

IN – intermittent flow, AN – annular flow

Fig. 5c-f show comparison between measured void fraction in upward and downward flow. The void fractions in downward flow were generally higher than those of upward flow for $x \leq 0.3$ and the difference in void fraction diminishes with both mass flux and vapor quality. The results are consistent with flow visualization and the difference in void fraction is directly linked to gravity effect with a longer residence time of the vapor phase in the test section in downward flow relative to upward flow.

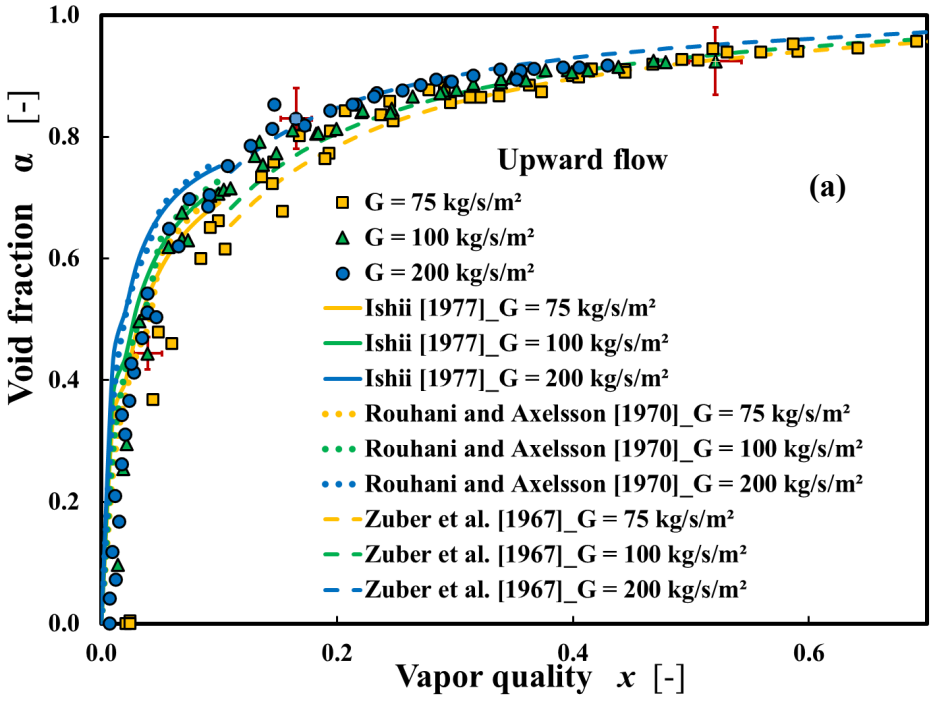

(b)

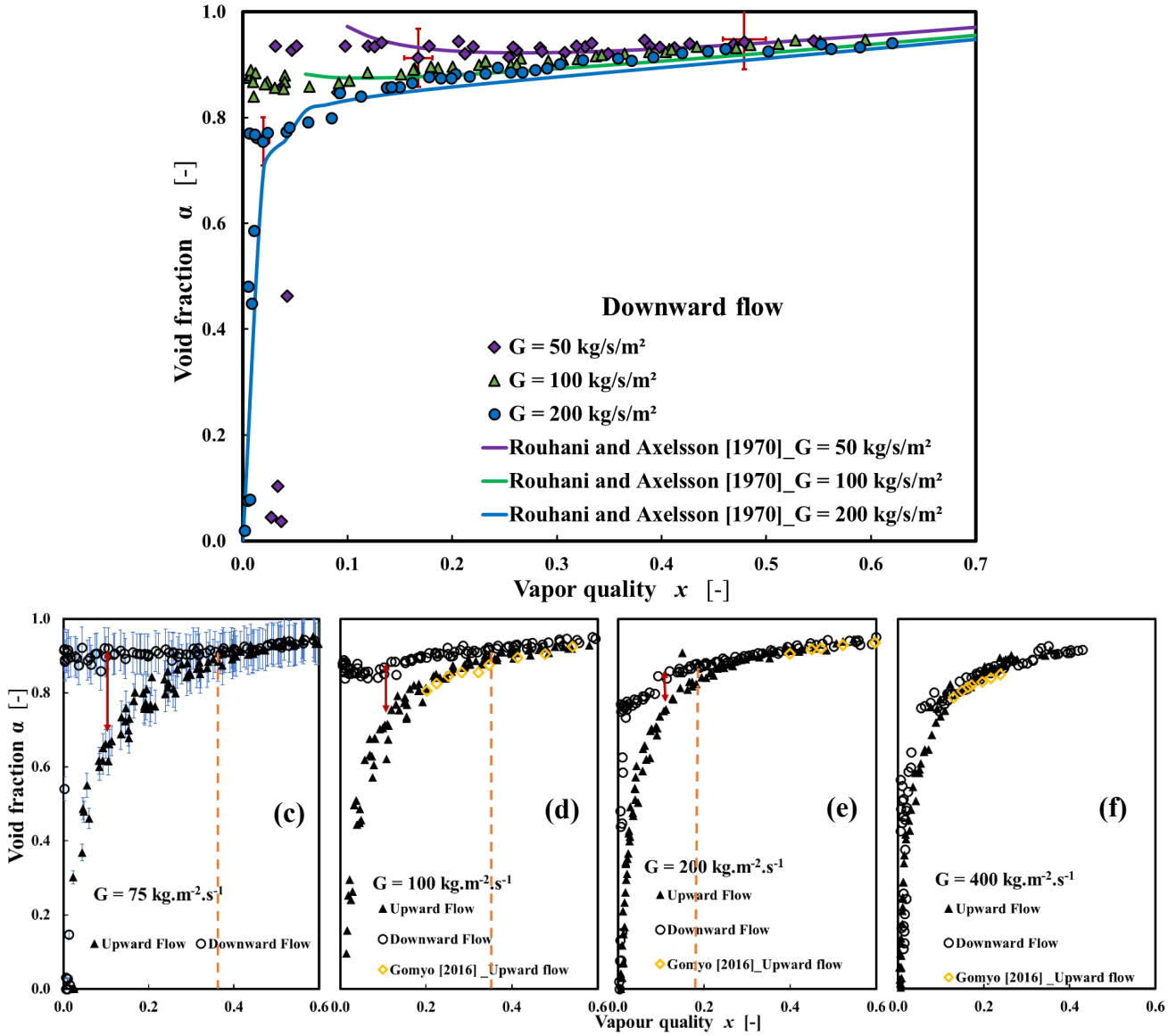

Figure 5. Void fraction versus vapor quality in upward and downward flow and comparison with selected models. Error bars were only put at selected point to improve readability.

The liquid film thickness (δ) in the falling film and annular flow regime were calculated from the measured void fraction using Eq. 16. In the current work, for $G \leq 400\, kg/m^2 s$, the contribution of liquid entrainment to the calculated liquid film thickness was negligible as shown by Narcy et al. (2014), using the model of Cioncolini et al. (2009) to estimate the droplet entrainment rate. Namely for the highest mass flux G=400 $kg/m^2/s$ and the highest quality x=0.4, the liquid entrainment rate e=0.2. Thus the difference in the estimation of the film thickness with and without entrainment is 0.1%, much below the uncertainty in the film thickness measurement itself. Figs. 6a and 6b show calculated film thickness in upward and downward flows respectively. Film thickness decreased with vapor quality as well as mass flux in upward flow. In downward flow, film thickness decreased with vapor quality but increased with mass flux. Predicted void fraction in the annular flow regime using models of Zuber et al. (1967) (upward flow) and Rouhani and Axelsson (1970) (downward flow) were also used to estimate the liquid film thickness according to Eq. 16. The predicted liquid film

thickness agrees favorably with experimental results (Fig. 6). The mean absolute error for both models are 14.9% (Zuber et al. (1967) – upward flow) and 16.1% (Rouhani and Axelsson (1970) - downward flow).

$$\delta = 0.5D(1 - \sqrt{\alpha}) \tag{16}$$

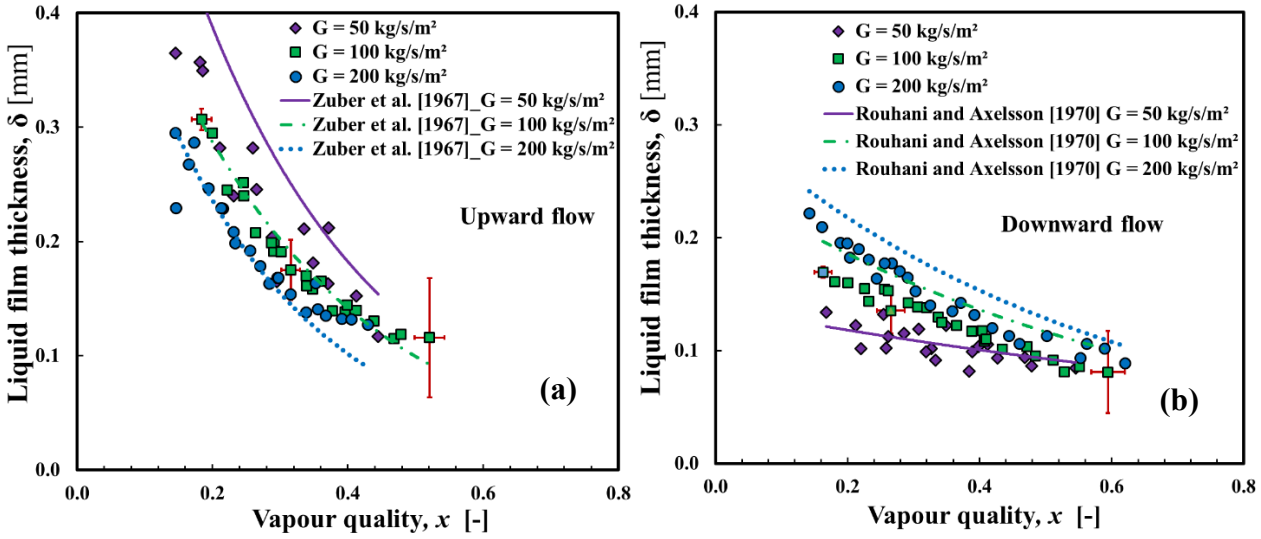

Figure 6. Liquid film thickness versus vapor quality, a. upward flow, b. downward flow.

3.3 Vapor velocity

Measured void fraction at the outlet of the heated test section was used to compute vapor velocity in both upward and downward flows over a wide range of quality corresponding to subcooled and saturated boiling regimes. Figs. 7 and 8 show computed vapor velocity versus mixture velocity for upward and downward flows respectively. Due to lack of precision in the quality for very low values of the quality corresponding to bubbly flow, only vapor velocities corresponding to intermittent, falling film (downward flow) and annular flow are presented. Figs. 7a-b show vapor velocity in the intermittent and annular flow regimes respectively along with comparison with relevant models. A good agreement can be seen between experimental and predicted vapor velocity, although the data showed higher dispersion in the intermittent flow regime. Figs. 8a-c show computed vapor velocity versus mixture velocity in downward flow for intermittent, falling film and annular flow regimes respectively along with comparison with the model of Rouhani and Axelsson (1970). Good agreement is seen between experimental and predicted vapor velocity for all flow regimes and vapor quality.

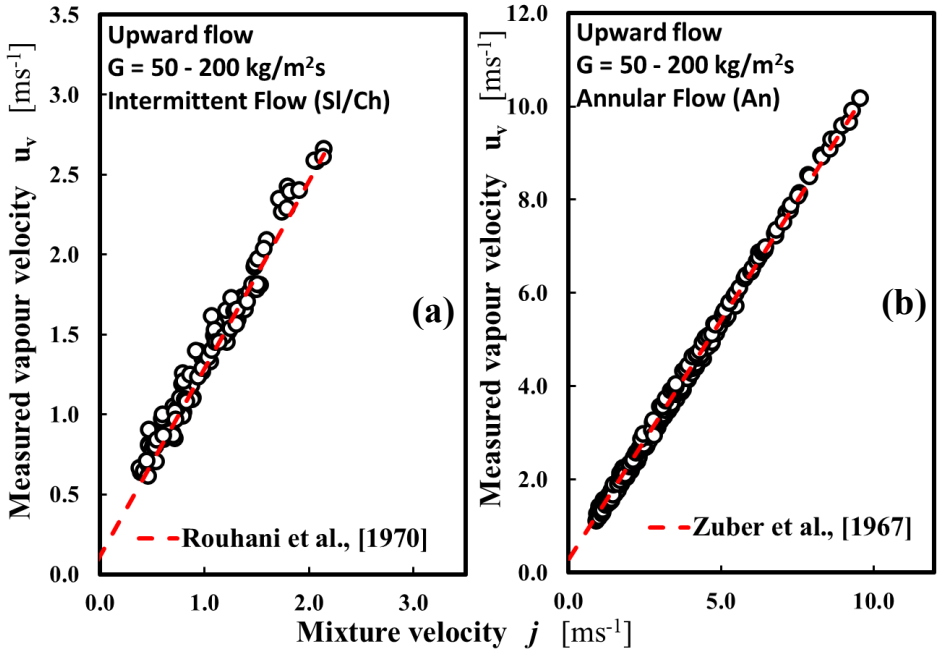

Figure 7. Vapor velocity versus mixture velocity in upward flow.

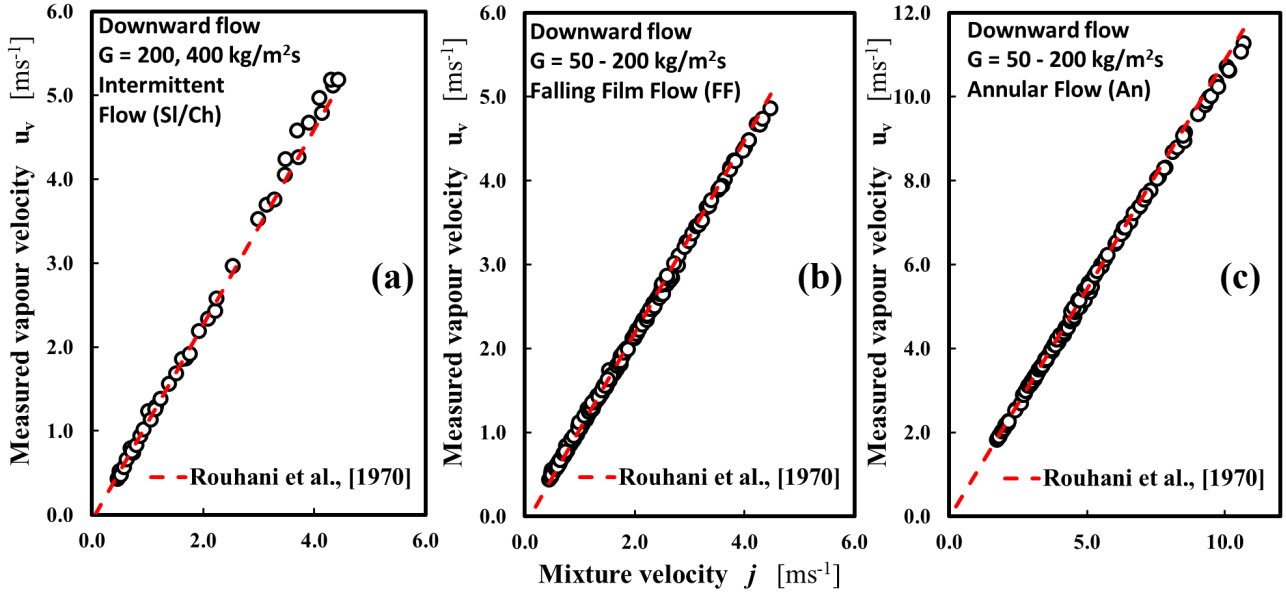

Figure 8. Vapor velocity versus mixture velocity in downward flow.

3.4 Wall shear stress and heat transfer coefficient

Results of measured heat transfer coefficient and wall shear stress for flow boiling under various conditions of inlet vapor quality, heat flux and mass flux are presented in terms of mean vapor quality for both upward and downward flows (Fig. 9). The heat transfer coefficient and wall shear stress increased with both vapor quality and mass flux in both upward and downward flows. Both the heat transfer coefficient and wall shear stress also increased with the wall heat flux for the same mean vapor quality in both upward and downward flows. This heat flux dependence was predominant in the nucleate boiling regimes; nucleate boiling (NB), nucleate boiling in the falling-film (NBFF) and

nucleate boiling in the annular flow (NBA). This is consistent with recent reports in flow boiling (Kim and Mudawar, 2013b, 2013a; Layssac, 2018). In most of the experiments, except for $G = 400\ kg/m^2s$, bubble nucleation at the wall was observed from the flow visualizations. These observations are in agreement with the measured values of the wall temperature T_w that are larger than the temperature for the onset of nucleated boiling T_{w_ONB} given by Davis and Anderson (1966):

$$(T_w)_{ONB} = T_{sat} + \frac{8\sigma q_{ONB} T_{sat}}{h_{lv}\lambda_l \rho_l} \tag{17}$$

The nucleated bubbles at the wall seem to act as a roughness at the wall leading to an increase of the velocity gradient of liquid near the wall and an increase of the friction velocity. The effect of heat flux was generally higher in downward flow relative to upward flow. This is likely due to longer residence time of nucleated bubbles attached at the wall in downward flow which in turn increases the time-averaged apparent roughness at the wall relative to upward flow. Namely, in upward flow drag force and buoyancy force are in the same direction and promote the bubble detachment whereas in downward flow they are in the opposite direction. The range of mixture velocity over which the effect of heat flux was significant was also wider in downward flow relative to upward flow. This is attributed to the wider range of mixture velocity for which nucleate boiling regimes (NB, NBFF and NBA) occurred in downward flows relative to upward flow. Overall, there was a strong coupling between the wall shear stress and wall heat transfer in both upward and downward flows. Modelling results on the wall shear stress and heat transfer coefficient will be discussed in the next sections.

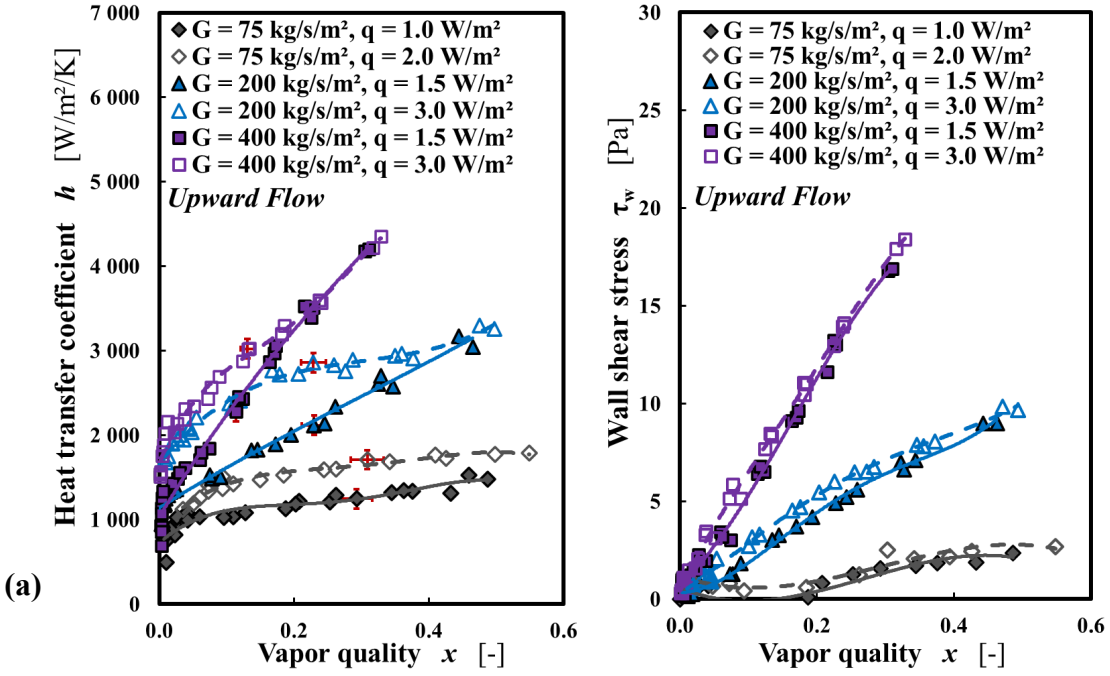

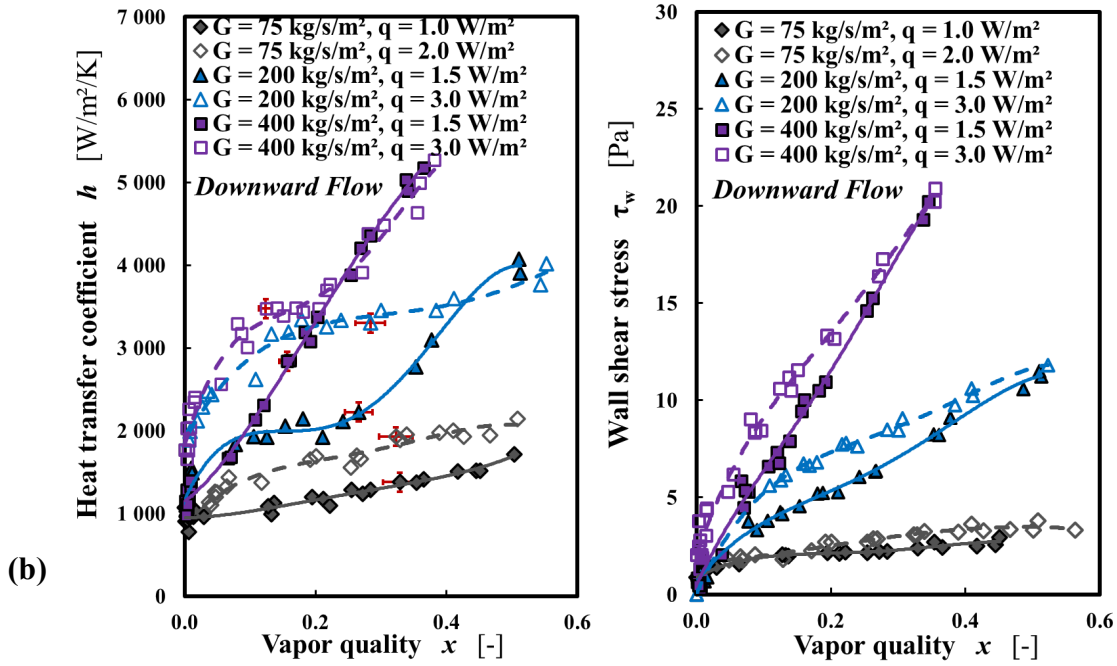

Figure 9. Evolutions of the heat transfer coefficient and wall shear stress for different mass and heat fluxes, a. upward flow, b. downward flow; heat transfer coefficient (left), wall shear stress (right). The lines are polynomial fits that provide trends: upward flow (solid lines), downward flow (dashed lines).

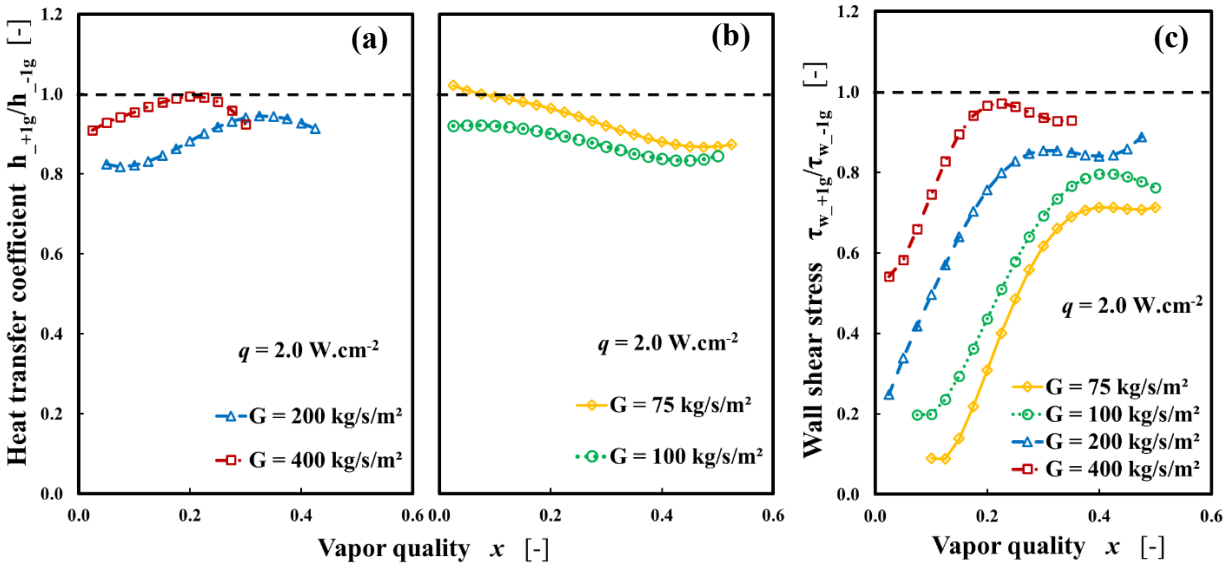

Figure 10. a-b. Ratio of heat transfer coefficient in $+1g$ (upward flow) to heat transfer coefficient in $-1g$ (downward flow), c. Ratio of wall shear stress in $+1g$ to wall shear stress in $-1g$.

Fig. 10 and Table 4 provide comparisons between heat transfer coefficient in upward and downward flow at constant heat flux and selected mass fluxes along with the corresponding wall shear stress. At constant heat flux, both the heat transfer coefficient and wall shear stress were generally higher in downward flow. This is linked to the higher liquid velocity in downward flow relative to upward

flow. In the case of wall shear stress, the ratio increased with increase in mass flux and vapor quality (Fig. 10c). This trend was replicated for measured heat transfer coefficient for $G = 200$ and $400\ kg/m^2/s$ (Fig. 10a), while the reverse was the case at lower mass flux (Fig. 10b). As inertia becomes dominant compared to gravity ($G = 400\ kg/m^2/s, x \geq 0.15$), heat transfer coefficient and wall shear stress in upward and downward flows become comparable. For $G = 400\ kg/m^2/s$, the Froude number $Fr = G^2/\rho_l^2 g\ D = 1.34$. This number is lower than 1 for $G \leq 200\ kg/m^2/s$.

Table 4. Ratio of heat transfer coefficient and wall shear stress between upward and downward flows for $q = 1.0$ and $2.0\ W/cm^2$.

Heat transfer coefficient				
Mass flux	$q = 1.0\ W/cm^2$		$q = 2.0\ W/cm^2$	
	$x = 0.10$	$x = 0.35$	$x = 0.10$	$x = 0.35$
$\boldsymbol{G = 75\ kg/m^2/s}$	1.10	0.96	0.99	0.90
$\boldsymbol{G = 100\ kg/m^2/s}$	0.99	1.03	0.92	0.85
$\boldsymbol{G = 200\ kg/m^2/s}$	1.00	0.94	0.82	0.94
$\boldsymbol{G = 400\ kg/m^2/s}$	–	–	0.96	0.92
Wall shear stress				
Mass flux	$q = 1.0\ W/cm^2$		$q = 2.0\ W/cm^2$	
	$x = 0.10$	$x = 0.35$	$x = 0.10$	$x = 0.35$
$\boldsymbol{G = 75\ kg/m^2/s}$	0.20	0.72	0.09	0.69
$\boldsymbol{G = 100\ kg/m^2/s}$	0.19	0.76	0.20	0.77
$\boldsymbol{G = 200\ kg/m^2/s}$	0.56	0.89	0.5	0.85
$\boldsymbol{G = 400\ kg/m^2/s}$	–	–	0.75	0.93

3.4.1. Modelling of wall shear stress for non-boiling vapor-liquid two-phase flow

At saturated inlet conditions, the fluid enters the test section as vapor-liquid two-phase flow. The saturated boiling regime corresponds mostly to annular flow with limited range of intermittent flow. With no heat flux applied to the test section, the wall shear stress corresponds to adiabatic two-phase flow. The wall shear was generally higher in downward flow for $G \leq 200\ kg/m^2s$ (See Fig. A2 in Appendix).

The adiabatic data were compared to correlations of Muller-Steinhagen and Heck (1986) (Eq. 18) and Kim & Mudawar (2012) (Eqs. 19-23). Both correlations gave similar predictions over the range of test conditions and gave good prediction the measured data within $\pm 30\%$. However, the correlations underpredicted the measured wall shear stress in both upward and downward flows for $G \leq 200\ kg/m^2s$ and provided good estimation of the measured data at $G = 400\ kg/m^2s$ (Fig. 11). To improve model performance, modification of the correlation of Kim & Mudawar (2012) was proposed by introducing the Martinelli parameter (X) and small modifications to the coefficients in their expression for C_A (see Table 5). The proposed correlation provided good prediction of the

measured wall shear stress over the measurement range in both upward and downward flows. Although, the correlation for downward flow underpredicted the measured data for $G < 100\ kg/m^2s$.

$$\left(\frac{dp}{dz}\right)_{fr} = F(1-x)^{1/3} + Bx^3 \quad 18$$

where $F = A + 2(B-A)x$, $A = \left(\frac{dp}{dz}\right)_{lo}$, $B = \left(\frac{dp}{dz}\right)_{vo}$, $\left(\frac{dp}{dz}\right)_{lo} = -f_{lo}\frac{2G^2}{\rho_l D}$, $\left(\frac{dp}{dz}\right)_{vo} = -f_{vo}\frac{2G^2}{\rho_v D}$

$$\left(\frac{dp}{dz}\right)_{fr} = \frac{4\tau_{w\_2\emptyset}}{D} = \emptyset_l^2\left(\frac{dp}{dz}\right)_l \quad 19$$

$$\emptyset_l^2 = 1 + \frac{C_A}{X} + \frac{1}{X^2} \quad 20$$

$$X = \left[\left(\frac{dp}{dz}\right)_l \Big/ \left(\frac{dp}{dz}\right)_v\right]^{0.5} \quad 21$$

$$\left(\frac{dp}{dz}\right)_l = -\frac{4}{D}f_l\frac{\rho_l j_l^2}{2} = -f_l\frac{2G^2(1-x)^2}{\rho_l D} \quad 22$$

$$\left(\frac{dp}{dz}\right)_v = -\frac{4}{D}f_v\frac{\rho_v j_v^2}{2} = -f_v\frac{2G^2x^2}{\rho_v D} \quad 23$$

Table 5. Expressions for C_A and f_k.

Kim & Mudawar (2012)	$f_k = \begin{cases} 16Re_k^{-1} & Re_k < 2000 \\ 0.079Re_k^{-0.25} & 2000 \le Re_k < 20000 \\ 0.046Re_k^{-0.2} & Re_k \ge 20000 \end{cases}$
	$C_A = \begin{cases} 0.39Re_{lo}^{0.03}Su_{vo}^{0.1}(\rho_l/\rho_v)^{0.35}, & Re_l \ge 2000, Re_v \ge 2000 \\ 8.7\times10^{-4}Re_{lo}^{0.17}Su_{vo}^{0.1}(\rho_l/\rho_v)^{0.14}, & Re_l \ge 2000, Re_v < 2000 \\ 0.001559Su_{vo}^{0.1}(\rho_l/\rho_v)^{0.36}, & Re_l < 2000, Re_v \ge 2000 \\ 3.5\times10^{-5}Re_{lo}^{0.44}Su_{vo}^{0.1}(\rho_l/\rho_v)^{0.5}, & Re_l < 2000, Re_v < 2000 \end{cases}$
Proposed corr. (A) for upward flow	$f_k = \begin{cases} 16Re_k^{-1} & Re_k < 1500 \\ 0.079Re_k^{-0.25} & 1500 \le Re_k < 20000 \\ 0.046Re_k^{-0.2} & Re_k \ge 20000 \end{cases}$
	$C_A = \begin{cases} 0.33Re_{lo}^{0.03}Su_{vo}^{0.1}(\rho_l/\rho_v)^{0.35}(1/X^{0.22}), & Re_l \ge 3000, Re_v \ge 3000 \\ 0.40Re_{lo}^{0.03}Su_{vo}^{0.1}(\rho_l/\rho_v)^{0.35}(1/X^{0.27}), & Re_l < 3000, Re_v \ge 3000 \end{cases}$
Proposed corr. (A) for downward flow	$C_A = \begin{cases} 0.38Re_{lo}^{0.03}Su_{vo}^{0.1}(\rho_l/\rho_v)^{0.35}(1/X^{0.22}), & Re_l \ge 3000, Re_v \ge 3000 \\ 0.47Re_{lo}^{0.03}Su_{vo}^{0.1}(\rho_l/\rho_v)^{0.35}(1/X^{0.30}), & Re_l < 3000, Re_v \ge 3000 \end{cases}$

where k stands for liquid (l) or vapor (v), $Re_l = \frac{G(1-x)D}{\mu_l}$, $Re_{lo} = \frac{GD}{\mu_l}$, $Re_v = \frac{GxD}{\mu_v}$, $Re_{vo} = \frac{GD}{\mu_v}$, $Su_{vo} = \frac{\rho_v\sigma D}{\mu_v^2}$.

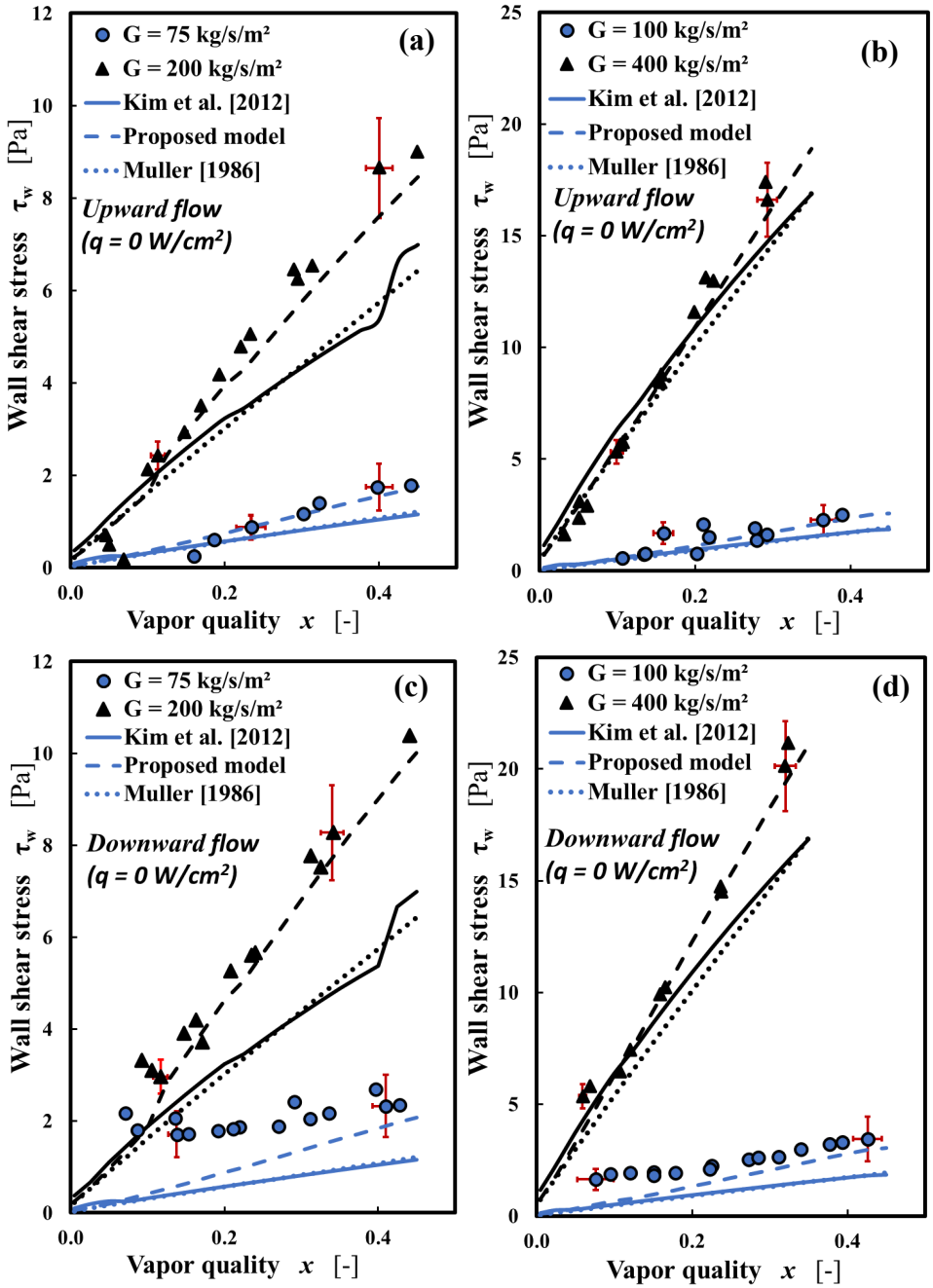

Figure 11. Comparison between measured wall shear stress for non-boiling two-phase flow with predicted wall shear stress obtained from selected correlations.

3.4.2. Modelling of wall shear stress in flow boiling (non-adiabatic)

Measured wall shear stress in upward and downward flow boiling were also compared to selected models for adiabatic flows two-phase flows (Fig. 12). The models of Muller-Steinhagen and Heck (1986) (Eq. 18) and Kim & Mudawar (2012) (Eqs. 19-23) generally under-predicted the wall shear stress for $G \leq 200\ kg/m^2s$ especially for downward flows. Although, these models provided good predictions of the wall shear stress at $G = 400\ kg/m^2s$, they failed to highlight the heat flux

dependence of the wall shear stress. This is expected, considering the fact that the models were developed for adiabatic two-phase flows. In comparison, the proposed model (Proposed corr. (A)-upward flow" in Table 4) for adiabatic two-phase flow gave better prediction of the wall shear stress over the entire range of mass fluxes. However, this correlation also failed to capture the effect of heat flux on the wall shear stress. Other models were also tested and mean square errors for all the models tested is provided in Table 6.

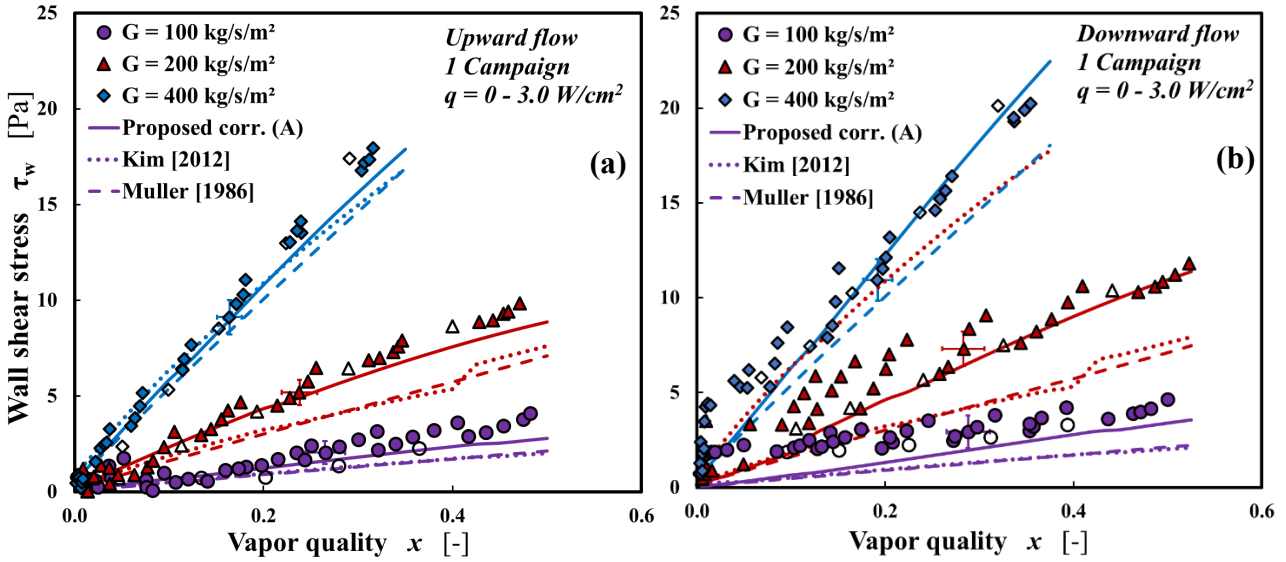

Figure 12. Wall shear stress versus vapor quality for vapor-liquid upward flow (left) and downward flow (right) along with comparison with selected models; adiabatic flow (open symbols), boiling flow (closed symbols).

Table 6. Mean absolute error for selected wall shear stress models applied to upward flow data

Model/Correlation	Upward (MAE %)	Downward (MAE %)
Lockhart and Martinelli (1949)	62.9	69.5
Friedel (1979)	70.4	65.1
Muller-Steinhagen and Heck (1986)	49.1	64.2
Cicchitti et al. (1960)	48.0	62.8
Cioncolini et al. (2009)	34.0	33.9
Cioncolini and Thome (2017)	32.0	22.7
Kim & Mudawar (2012b)	37.2	50.8
Kim & Mudawar (2013b)	32.9	37.6
Proposed corr. (A)	26.3	30.3
Proposed corr. (NA)	17.0	18.8

A – adiabatic, NA – flow boiling (non-adiabatic)

To account for the effect of wall heat flux on the wall shear stress in flow boiling, Kim & Mudawar (2013b) proposed a modification to the constant (C_A) in the model of Kim & Mudawar (2012). This

was done by introducing a function which depends on the boiling number (Bo) and Weber number of the liquid (We_{lo}) (Eq. 24).

$$C_{NA} = \begin{cases} C_A[1 + 60We_{lo}^{0.32}Bo^{0.78}] & Re_l \geq 2000 \\ C_A\left[1 + 530We_{lo}^{0.52}Bo^{1.09}\right] & Re_l < 2000 \end{cases} \quad 24$$

$$We_{lo} = \frac{G^2 D}{\rho_l \sigma}, Bo = \frac{q_w}{G h_{lv}}$$

Fig. 13a provides a comparison between predicted and measured wall shear stresses for upward flow boiling. The correlation provided good predictions of the measured wall shear stress over a limited range of data and also highlighted the dependence of wall shear stress on heat flux. The model overpredicted the wall shear stress at $G = 400\ kg/m^2s$ and underpredicted the wall shear stress at $G = 75\ kg/m^2s$. More importantly, in the inertia dominant regime, measured data showed a suppression of the effect of wall heat flux. This suppression increased with both mass flux and vapor quality for $Re_l \geq 1500$. This trend in the experimental data is consistent with the conditions necessary for bubble nucleation at the wall. The model of Kim & Mudawar (2013b), failed to capture this trend (not shown for conciseness). Due to the above limitations to the model, a modification to the model was proposed in the current work. In the proposed correlation, C_A is determined according to "Proposed corr. (A)-upward flow" in Table 5. To account for the reduced heat flux dependence with increasing vapor quality, for $Re_l \geq 1500$, the Weber number of the liquid (We_{lo}) was replaced with liquid Weber number determined with the superficial velocity (We_l). Modifications were also done to the coefficients in Eq. 24 to give a better description of the heat flux dependence. The proposed correlation for C_{NA} is given by Eq. 25. Fig. 13b show comparisons between predicted and measured wall shear stresses in upward flow boiling. The correlation provided good predictions of the measured wall shear stress over the entire range of measurement. Furthermore, the proposed model recovered the trend of the measured data (not shown for conciseness). The mean square error for the model of Kim & Mudawar (2013b) and that for the proposed correlation are given in Table 6 above.

$$C_{NA} = \begin{cases} C_A[1 + 30We_l^{0.32}Bo^{0.78}] & Re_l \geq 1500 \\ C_A\left[1 + 320We_{lo}^{0.52}Bo^{1.09}\right] & Re_l < 1500 \end{cases} \quad 25$$

where $We_l = \frac{G^2(1-x)^2 D}{\rho_l \sigma}$.

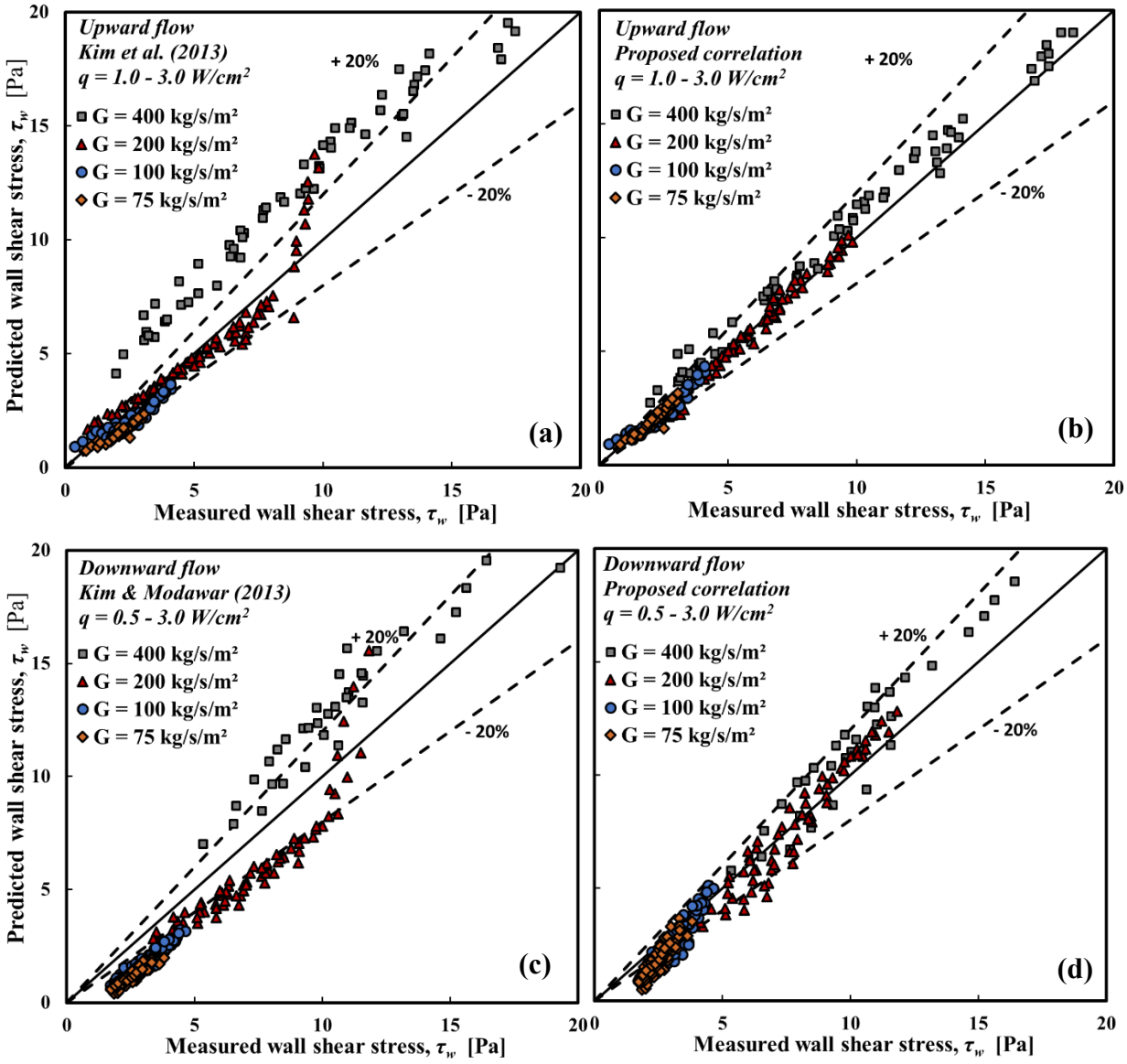

Figure 13. Comparison between measured and predicted wall shear stress in upward (top) and downward flow boiling: (a & c) model of Kim & Mudawar (2013b), (b & d) proposed correlation.

As described earlier, the measured wall shear stress was generally higher in downward flow relative to upward flow and so modifications were made to coefficients of C_{NA} proposed for upward flow (Eq. 25). In the proposed correlation for C_{NA} in downward flow, C_A is determined according to "Proposed corr. (A)-downward flow" in Table 5. The proposed correlation is given by Eq. 26. Fig. 13c provide comparisons of measured wall shear stress and wall shear stress computed from the model of Kim & Mudawar (2013b) (Eq. 24), as well as that computed from the proposed correlation for downward flow (Eq. 26). The model of Kim & Mudawar (2013b) underpredicted and overpredicted the measured data for $G \leq 200\ kg/m^2s$ and $G = 400\ kg/m^2s$ respectively. The proposed correlation provided a better prediction of the measured data, particularly for $G \geq 100\ kg/m^2s$. The mean square error for the model of Kim & Mudawar (2013b) and that for the proposed correlation are given in Table 6 above.

$$C_{NA} = \begin{cases} C_A[1 + 30We_l^{0.32}Bo^{0.78}] & Re_l \geq 1500 \\ C_A[1 + 400We_{lo}^{0.52}Bo^{1.09}] & Re_l < 1500 \end{cases} \quad 26$$

3.4.3 Modelling of heat transfer coefficient

As mentioned in the introduction, correlations for heat transfer based on the wall shear stress (or friction velocity) have been shown to provide good estimation of wall heat transfer. This is due to the coupling between wall heat transfer and wall shear stress. A correlation for heat transfer coefficient for annular convective flow based on the friction velocity was proposed by Cioncolini and Thome (2011). This correlation was developed from algebraic turbulent eddy diffusivity models for momentum and heat in the liquid film. The model is given by Eq. 27.

$$h = 0.0776\frac{\lambda_l}{\delta}(\delta^+)^{0.9}Pr^{0.52} \quad 10 < \delta^+ < 800 \qquad 0.86 < Pr < 6.1 \quad 27$$

$$\delta^+ = \frac{\delta}{y^+},\ y^+ = \frac{v_l}{u^*}, u^* = \left(\frac{\tau_w}{\rho_l}\right)^{0.5}, \delta = y^+.max\left[\sqrt{\frac{2\Gamma_{l,f}^*}{R^*}}; 0.0066\frac{\Gamma_{l,f}^*}{R^*}\right]$$

δ is the mean liquid film thickness, δ^+ is the dimensionless mean liquid film thickness, u^* is the friction velocity, y^+ is the dimensionless distance from the wall, R^* is the dimensionless tube radius and $\Gamma_{l,f}^*$ is the dimensionless mass flow rate in the liquid film. The correlation is applicable to water, refrigerants and selected hydrocarbons flowing inside vertical and horizontal tube with diameter in the range of $1.03 \leq D \leq 14.4\,mm$. The friction velocity was obtained from the wall shear stress correlation of Cioncolini et al. (2009) (Eq. 28). The model is valid for fully convective flows and does not account for the effect of wall heat flux on heat transfer. Fig. 14 shows comparison between measured heat transfer and predicted heat transfer using correlation of Cioncolini and Thome (2011) for both upward and downward flows. The correlation gave a fairly good prediction at the highest mass flux tested ($G = 400\ kg/m^2s$) where convective contribution to the heat transfer was dominant (Fig. 14b&d). It, however, fails to predict the heat transfer coefficient at lower mass fluxes where nucleate boing is the predominant mode of heat transfer (Fig. 14a&c).

$$\left(\frac{dp}{dz}\right)_{fr} = \frac{4\tau_{w\_2\emptyset}}{D} = 2f_{2\emptyset}\frac{\rho_c j_c^2}{D} \quad 28$$

$$f_{2\emptyset} = 0.172We_c^{-0.372} \quad 29$$

$$We_c = \frac{\rho_c j_v^2 D}{\sigma} \quad \left\{\rho_c = \frac{x + e(1-x)}{\frac{x}{\rho_v} + \frac{e(1-x)}{\rho_l}}\right\}$$

$$e = (1 + 271.6We_c^{-0.8395})^{-2.209}$$

were We_c is the core Weber number, e is the liquid entrainment rate and ρ_c is the core density

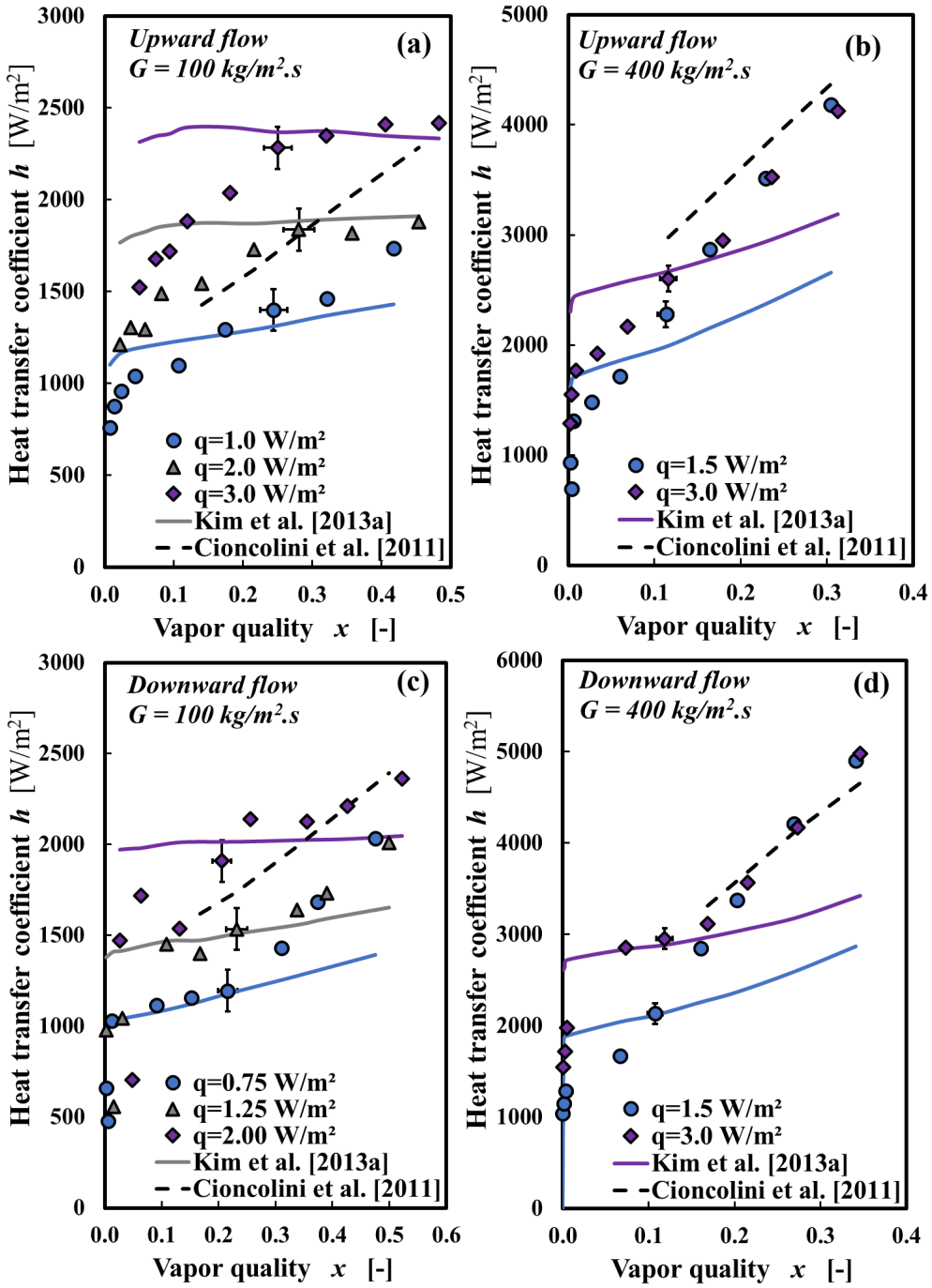

Figure 14. Comparison between measured heat transfer coefficient with correlations of Cioncolini and Thome (2011) and Kim and Mudawar (2013a) for $G = 100\ kg/m^2s$ (left) and $G = 400\ kg/m^2s$ (right); experiment (symbols), prediction (lines).

It is quite obvious from the foregoing that, heat transfer coefficient is influenced by wall heating in the nucleate boiling dominant regime. This explains the poor prediction of the model of Cioncolini and Thome (2011) in the nucleate boiling dominant regime. Kim and Mudawar (2013a) proposed an empirical correlation for predicting heat transfer coefficient which takes into account the nucleate and convective boiling contributions to the total heat transfer. The correlation, which was developed

for saturated boiling regime, is given by Eqs. 30-32.

$$h_{2\emptyset} = \sqrt{\left({h_{nb}}^2 + {h_{cb}}^2\right)} \tag{30}$$

$$h_{nb} = h_l \left[C_1 Bo^{C_2} \left(\frac{P}{P_{crit}}\right)^{C_3} (1-x)^{C_4} \right] \tag{31}$$

$$h_{cb} = h_l \left[C_5 Bo^{C_6} We_{lo}^{C_7} + C_8 \left(\frac{1}{X_{tt}}\right)^{C_9} \left(\frac{\rho_v}{\rho_l}\right)^{C_{10}} \right] \tag{32}$$

where $C_1 - C_{10}$ are empirical constants (see Table 7), Bo is the Boiling number, X_{tt} is the Lockhart–Martinelli parameter based on turbulent liquid-turbulent vapor flows, We_{lo} is the Weber number of the liquid, x is the vapor quality, P/P_{crit} is the reduced pressure, h_l is determined from single-phase turbulent heat transfer correlation of Dittus and Boelter (1930).

$$Bo = \frac{q}{Gh_{lv}}, X_{tt} = \left(\frac{1-x}{x}\right)^{0.9} \left(\frac{\rho_v}{\rho_l}\right)^{0.5} \left(\frac{\mu_l}{\mu_v}\right)^{0.1}, We_{lo} = G^2 D/(\sigma \rho_l), h_l = 0.023 Re_l^{0.8} Pr_l^{0.4} \frac{\lambda_l}{D}$$

This correlation is applicable to refrigerants flowing inside vertical tubes of diameter 4.5 to 6.50 mm with mass flux of 100 to 500 kg/m^2s. In their correlation, h_l is determined using $Re_l = G(1-x)D/\mu_l$ not $Re_{lo} = GD/\mu_l$. The term $(1-x)^{C_4}$ was introduced to account for nucleate boiling suppression, while We_{lo} accounts for the interaction between inertia and surface tension forces.

The nucleate boiling heat transfer (h_{nb}) given by Eq. 31 is dependent of mass flux and decreases slightly with quality. The first term in the bracket in the expression of h_{cb} (Eq. 32) is generally small due to the small value of the exponent of Bo. h_{cb} increases with both mass flux and vapor quality. The correlation generally over-predicted the measured heat transfer in the nucleate boiling regime (Fig. 14) particularly for upward flow. The over-prediction in the nucleate boiling regime can be explained by the relatively fewer nucleation sites in the Sapphire tube used in the current work (relative to metallic tubes). The density of active nucleation sites was measured from high-speed video recording and was about 1 to 2 active sites per cm^2 for the bubbly flows with a wall superheat of 3 to 4 K (see the video in the supplementary material). An estimation of the active site density through the classical correlation of Kocamustafaogullari and Ishii (1983) gave values for metallic surfaces around 10 sites per cm^2. This difference is likely linked to the surface roughness R_a. In general, the surface roughness of sapphire substrates, $0.3 \leq R_a \leq 0.7\ nm$, (Shang Ying-Qi et al., 2017) is significantly lower than that of common copper substrates, $0.1 \leq R_a \leq 10\ \mu m$, (Wang et al., 2018). At high vapor quality in upward flow, their model gave good predictions of the measured heat transfer at lower mass flux ($G \leq 100\ kg/m^2s$) (Fig. 14a) and under-predicted the measured heat transfer at higher mass flux ($G \geq 200\ kg/m^2s$) (Fig. 14b). Furthermore, in their model, the contribution of nucleate boiling to the total heat transfer remained significant even at high mass fluxes/high vapor quality where convective heat transfer is expected to become dominant (Fig. 14b). At high vapor quality in downward flow, their model under-predicted the measured heat transfer for

all mass fluxes. Experimental data was also compared to other heat transfer models. Table 8 provides a summary of the MAE for the various models. Overall, the model of Liu and Winterton (1991) gave the lowest value of MAE.

Table 7. Model coefficients for $h_{2\emptyset}$

Function	C_1	C_2	C_3	C_4	C_5	C_6	C_7	C_8	C_9	C_{10}
Kim's correlation	2345	0.70	0.38	-0.51	5.2	0.08	-0.54	3.5	0.94	0.25
Upward flow correlation	2345	0.76	0.38	-0.7	5.2	0.08	-0.54	5.1	0.71	0.13
Downward flow correlation	2345	0.76	0.38	-0.7	5.2	0.08	-0.54	5.5	0.71	0.13

Table 8. Mean absolute error for selected heat transfer models

Model/Correlation	Upward (MAE %)	Downward (MAE %)
Kandlikar (1990)	69.8	65.8
Kim and Mudawar (2013)	24.7	25.5
Kew and Cornwell (1997)	30.4	27.1
Cioncolini and Thome (2011)	14.1	17.7
Liu and Winterton (1991)	12.9	21.8
Proposed correlation	12.1	15.9

Due to the limitations of the model of Kim and Mudawar (2013a) described above, a modification to their model was done to improve the performance of the correlation in relation to the current work. This was done by small modifications of some of the empirical constants in the original model of Kim and Mudawar (2013a) for upward flow. The empirical constants of the proposed correlation are provided in Table 8 along with the empirical constants of the model of Kim and Mudawar (2013a). In the proposed correlation for upward flow, the evolution of nucleate and convective boiling contributions to the total heat transfer were similar to that of Kim and Mudawar (2013). However, the nucleate boiling contribution to the total heat transfer was lower and the convective boiling contribution to the total heat transfer was higher. The proposed correlation gave good prediction of the measured heat transfer in upward flow over the entire range of mass flux, heat flux and vapor quality (Fig. 15a-b). Due to the higher liquid velocity in downward flow relative to upward flow, the proposed model for upward flow was modified by increasing the multiplier of the convective part (i.e., C_8) from 5.1 to 5.5 (Table 7). Fig. 15c-d give comparisons between measured and predicted heat transfer coefficient in downward flow. The model gave good prediction of the measured data over the entire measurement conditions in downward flow.

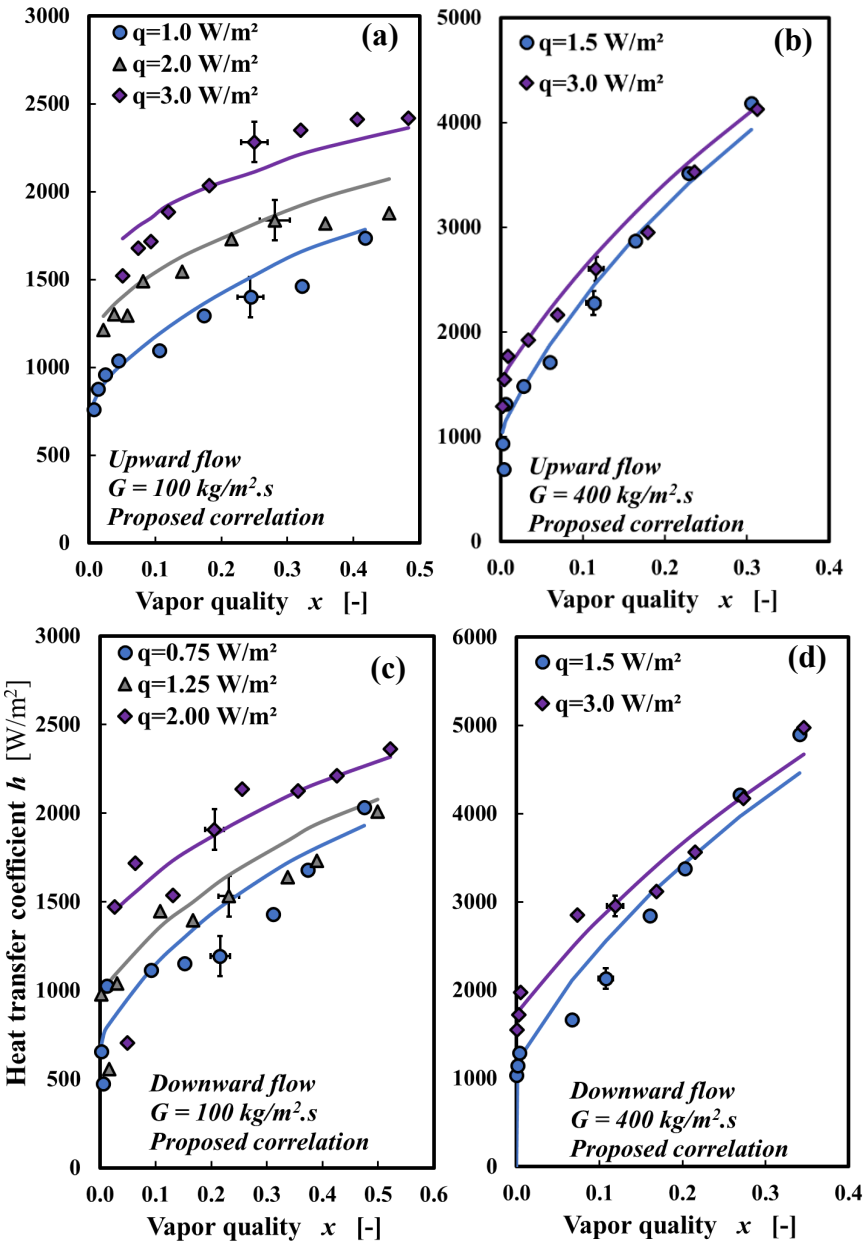

Figure 15. Comparison between measured heat transfer and that predicted using the proposed correlation for $G = 100\ kg/m^2s$ and $G = 400\ kg/m^2s$; experiment (symbols), prediction (lines).

3.5 Interfacial shear stress and wave structures

3.5.1 Interfacial shear stress

Fig. 16 provide comparisons between interfacial shear stress (τ_i) in upward and downward flows for various mass flux and constant heat flux. τ_i increased with mass flux in both flow configurations and was generally higher in upward flow. This is due to higher relative velocity between the vapor and liquid phases in upward flow. A ratio of τ_i in downward and upward flow is also provided in Table 9 to provide qualitative comparison. As mass flux increases, the ratio of τ_i between both configuration

increases (Fig. 16c and Table 9). Similar to wall shear stress, interfacial shear stress showed a dependence on heat flux, however, the dependence was less obvious (Fig. 17). The dependence of interfacial shear stress on wall heating was more significant downward flow (Fig. 17).

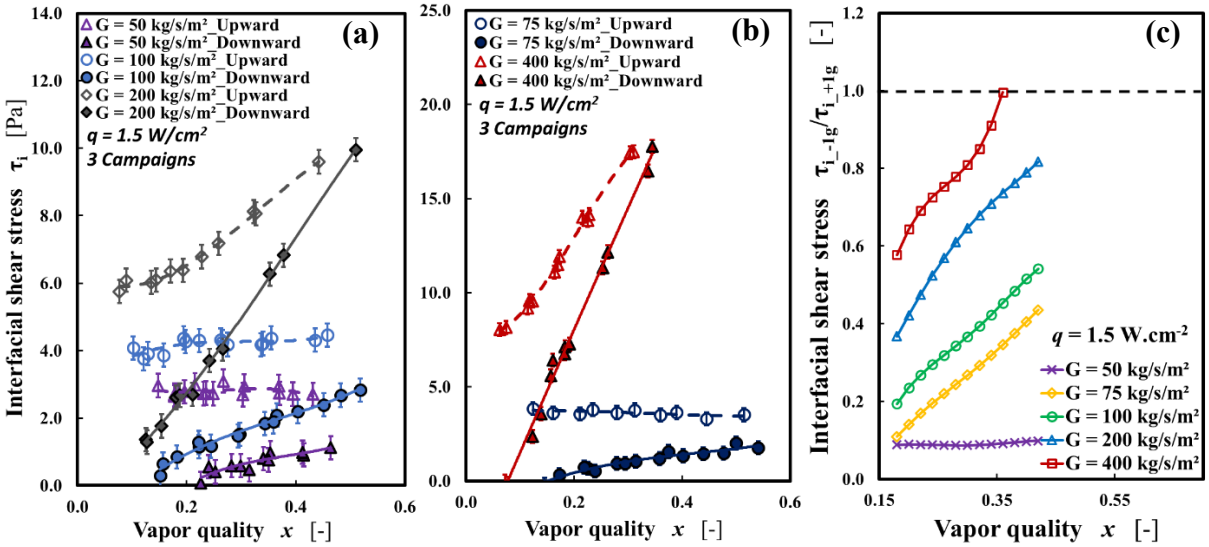

Figure 16. Comparison between interfacial shear stress in upward and downward flow at constant heat flux. The lines are polynomial fits that provide trends: upward flow (solid lines), downward flow (dashed lines).

Table 9. Ratio of interfacial shear stress between downward and upward flows for $q = 1.5$ and $3.0\ W/cm^2$.

Mass flux	$q = 1.5\ W/cm^2$		$q = 3.0\ W/cm^2$	
	$x = 0.20$	$x = 0.30$	$x = 0.10$	$x = 0.35$
$G = 50\ kg/m^2/s$	0.0895	0.0872	-	-
$G = 75\ kg/m^2/s$	0.1408	0.2680	-	-
$G = 100\ kg/m^2/s$	0.2335	0.3673	-	-
$G = 200\ kg/m^2/s$	0.4222	0.6469	0.966	0.7517
$G = 400\ kg/m^2/s$	0.6429	0.8092	0.6809	0.8854

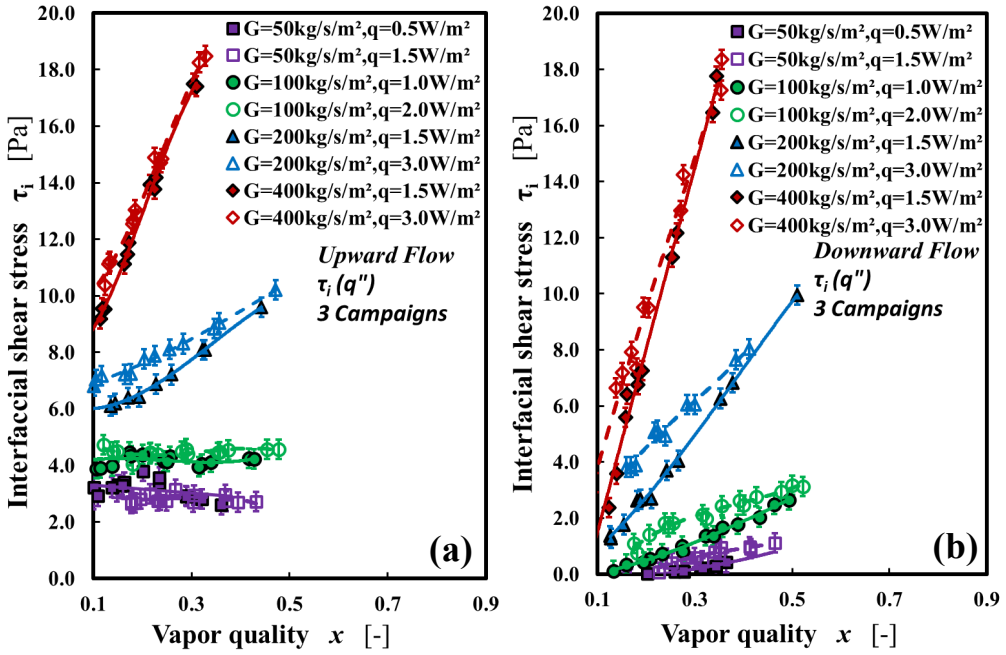

Figure 17. Interfacial shear stress versus vapor quality at selected heat flux in a. upward flow, b. downward flow. The lines are polynomial fits that provide trends: upward flow (solid lines), downward flow (dashed lines).

3.5.2 Modelling of interfacial friction factor

From the interfacial shear stress, it was possible to calculate the interfacial friction factor f_i from Eq 8 and to scale it by the friction factor of the vapor core flow f_v (Eq. 9). The values of f_i/f_v are plotted for upward flow in Fig. 18. The relative velocity between the phases in annular two-phase upward flow is often very high, resulting in the destabilization of the interface and emergence of roll waves (Belt et al., 2009; Narcy et al., 2014). The wavy liquid surface acts as a rough wall for the gas flow. Consequently, a number of models for predicting interfacial shear stress are analogical to wall friction factor correlations in rough pipes. Wallis (1969) proposed a correlation for interfacial factor for wavy annular films which was linked to the roughness of the interface (Eq. 33). It was assumed that the vapor core flow is fully turbulent and the roughness of the interface was equal to the liquid film thickness (δ). The correlation was developed from two-phase adiabatic flow using data obtained in large diameter tube ($D = 50\ mm$). In this flow configuration, the friction factor of the vapor core (f_v) flow is ≈ 0.005 and quite independent of the Reynolds number of the vapor. The model provided a good estimation of the measured interfacial friction factor ratio for $Re_v \geq 30{,}000$ (see Eq. 35) corresponding to $G = 400\ kg/m^2s$ ($x \geq 0.16$) and $G = 200\ kg/m^2s$ ($x \geq 0.35$) (Fig. 18a). This flow condition was characterized by high wave velocities and high wave frequencies which resulted in a significantly rough interface. Using a similar flow configuration to Wallis (1969), Belt et al. (2009) proposed a correlation given by Eq. 34. Their correlation over-predicted the friction factor ratio for $Re_v \geq 30{,}000$. Both correlations under-predicted the friction factor ratio for $Re_v < 30{,}000$. It was shown by Narcy et al. (2014) that for $Re_v < 30{,}000$ the turbulence in the vapor core flow is not fully developed. This explains the poor predictions of the model of Wallis (1969) and Belt et al.

(2009) for $Re_v < 30{,}000$. The regime corresponding to $Re_v < 30{,}000$, in the current work, represents a transition between smooth and fully rough turbulent regimes (Fore et al., 2000; Lopes and Dukler, 1986; Narcy et al., 2014). In the regime of transition between smooth and fully rough interface, Fore et al. (2000) highlighted the dependency of interfacial friction factor on both film thickness and Reynolds number of the gas phase. They introduced a function $(1 + A/Re_v)$ to the correlation of Wallis (1969) to account for the Reynolds number dependence. In the current work, the dependence of the friction factor ratio on the Reynolds number of the vapor is shown in Fig. 19b. A similar trend was also reported in the work of Narcy et al. (2014) for data acquired in an adiabatic section of the flow facility. Following similar approach to Fore et al. (2000), a function $(1 + A/Re_v^{1.3})$ was introduced (in the current work) to the model of Wallis, (1969). The exponent of Re_v was derived from a plot of f_i/f_v versus Re_v (Fig. 18b). A plot of f_i/f_v versus δ/D $(1 + 320000/Re_v^{1.3})$ is shown in Fig. 18c. As can be seen from Fig. 18c, the interfacial friction factor ratios collapsed into a single curve. A correlation for f_i/f_v in upward flow was proposed in terms of Re_v and δ/D (Eq. 35). The correlation gives a good prediction of the experimental data (Fig. 18d). It should be remarked that the interfacial friction factor ratio in downward flow showed significant dependence on the wall heat flux and modelling was done in relation to wave parameters in the next section.

$$\frac{f_i}{f_v} = 1 + 300\,{}^{\delta}/_{D} \tag{33}$$

$$f_i = 6.826 \times 10^{-4} + 2.316\,{}^{\delta}/_{D} \tag{34}$$

$$\frac{f_i}{f_v} = 1 + 215\,{}^{\delta}/_{D}\left(1 + {}^{3.2 \times 10^5}/_{Re_v^{1.3}}\right) \qquad \left(Re_v = \frac{U_v D_c}{\nu_v}, D_c = D\sqrt{\alpha}\right) \tag{35}$$

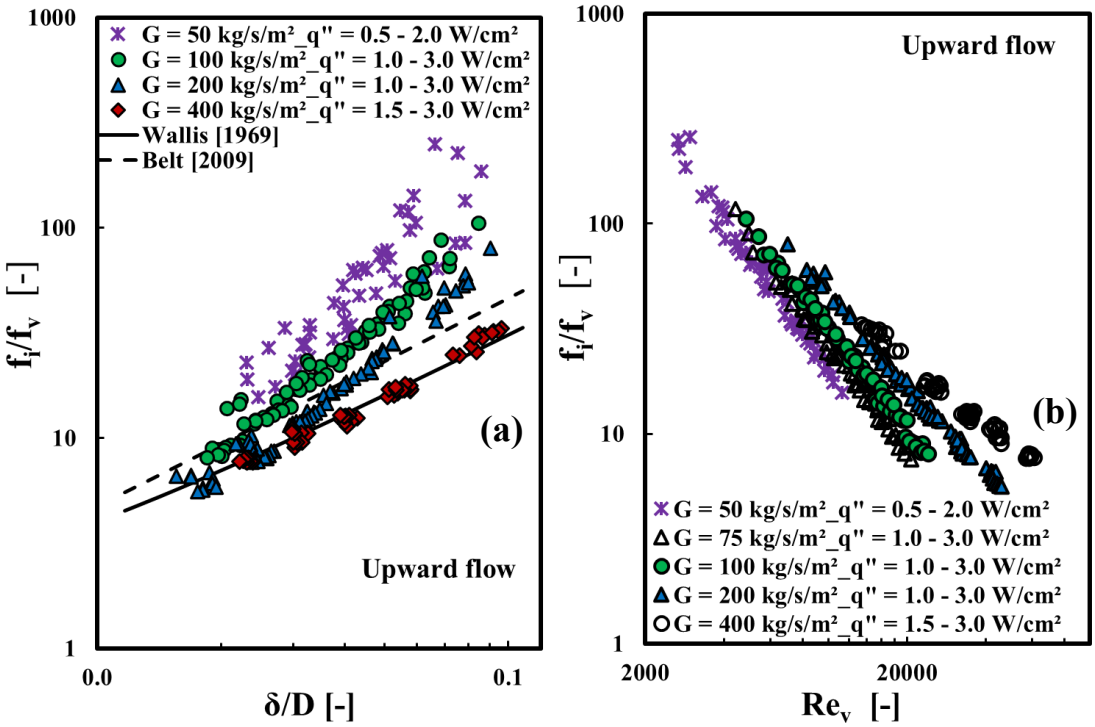

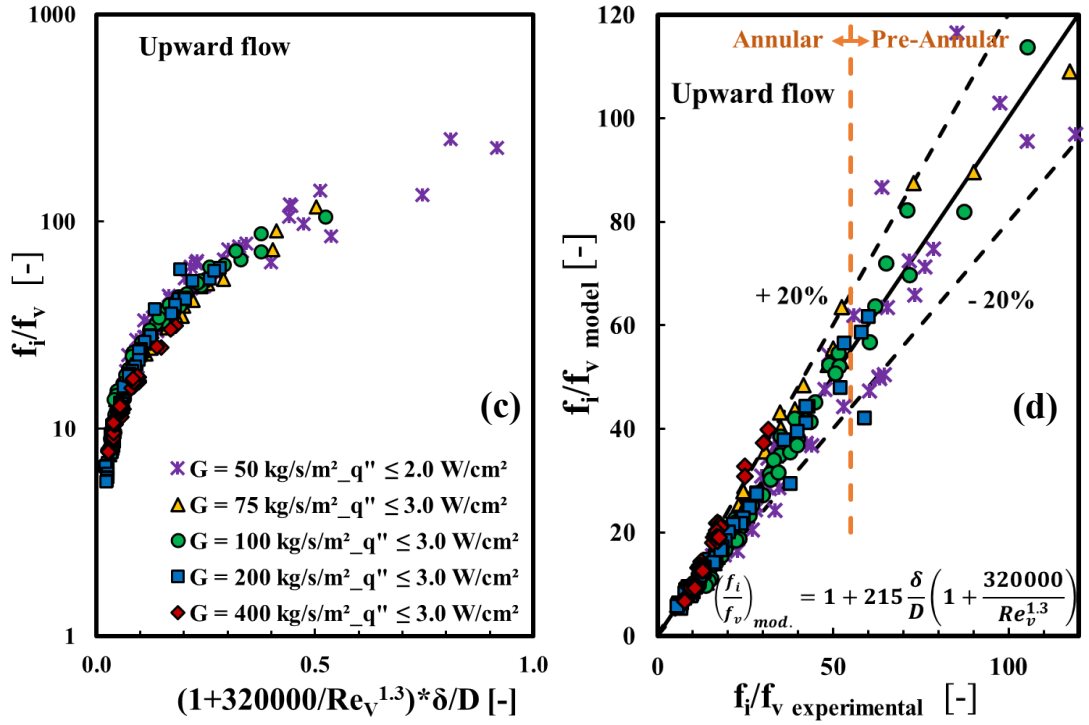

Figure 18. a. interfacial friction factor ratio versus dimensionless liquid film thickness, b. interfacial friction factor ratio versus Reynolds number of the vapor phase, c. interfacial friction factor ratio versus model function, and d. measured interfacial friction factor ratio versus predicted interfacial friction factor ratio.

3.5.3 Structure of the liquid film in annular flow: wave velocity and wave frequency

In this section, the structure of the interface, especially the velocity and the frequency of the roll waves are investigated. It is well known that the interfacial friction is directly linked to the interfacial structure. The void fraction probes used in this experiment did not have sufficient time and space resolution to measure the local real-time film thickness. Thus, the characterization of the interface was performed by image processing of high-speed visualizations and especially of the analysis of space-time diagrams.

Flow visualization revealed both roll waves and capillary waves (ripples) in upward and downward flows. The roll waves were more coherent and travelled at much higher velocities than the capillary waves. Fig. 19 show typical space time plots obtained from the time evolution of the grey levels on an axial line of the right image in the tube center. The roll waves in upward and downward flow configurations clearly appear as dark lines in the plots. The slope of the lines gives the wave velocity (U_w) and the intervals between them gives the period (T). Waves of different velocities merge along the test section in both flow configurations and there is intermittency in roll waves in downward flow configuration at low mass flux.

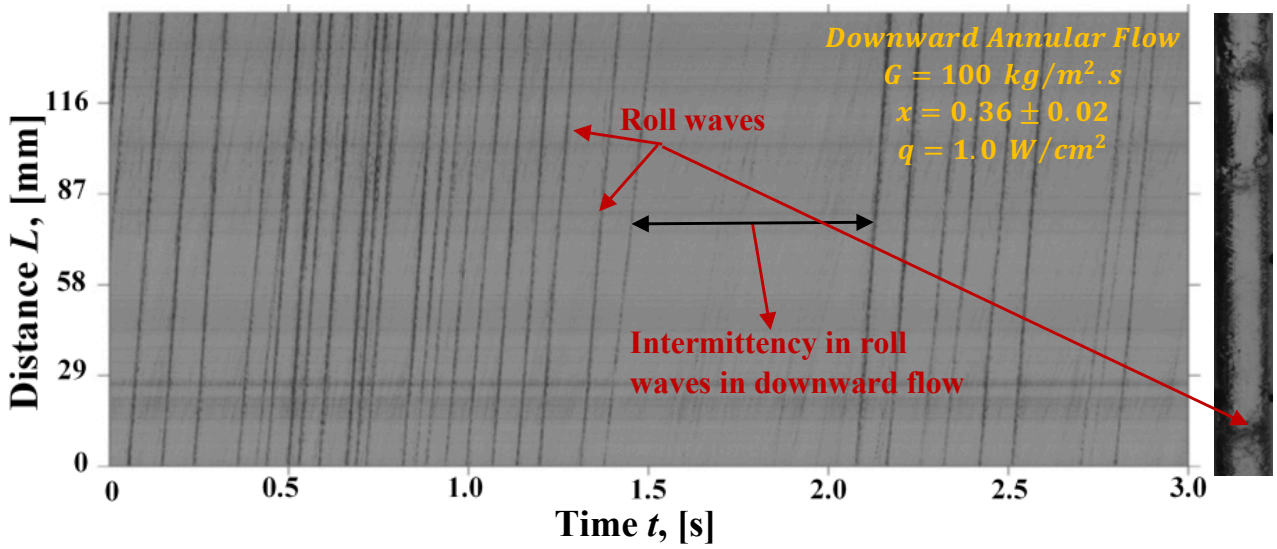

Figure 19. Typical distance versus time plot for annular downward flow at $G = 100\ kg/m^2s$.

In the current work $\geq$ 20,000 images were acquired at 1000 fps (and in some cases 1400 fps) for each flow condition corresponding to specific values of G, x and q. The total number of waves ranged from 400 for the lowest mass flux to 1200 for the highest mass flux. Image acquisition was carried out for two experimental campaigns at various inlet quality, mass flux and heat flux. Computed mean wave velocity and mean wave frequency from both campaigns converged within $\pm$7.5% of each other for similar flow condition. Image acquisition for each flow condition were also segmented into batches of $\approx$ 2500 images. For a given flow condition, computed wave frequency and wave velocity for each image batch were within $\pm$5% of the mean value obtained for the entire recording. The temporal interval between successive waves (period of wave) and consequently the wave frequency varied significantly. Typically range of the wave frequency was between 5 to 150 Hz. The variation of wave velocity among the individual waves (or group of 2-4 waves) was much smaller than the frequency variation (particular at higher flow rates). Fig. 20 shows typical histogram of wave frequency and wave velocity at selected flow conditions. The histogram provides further validation of data convergence.

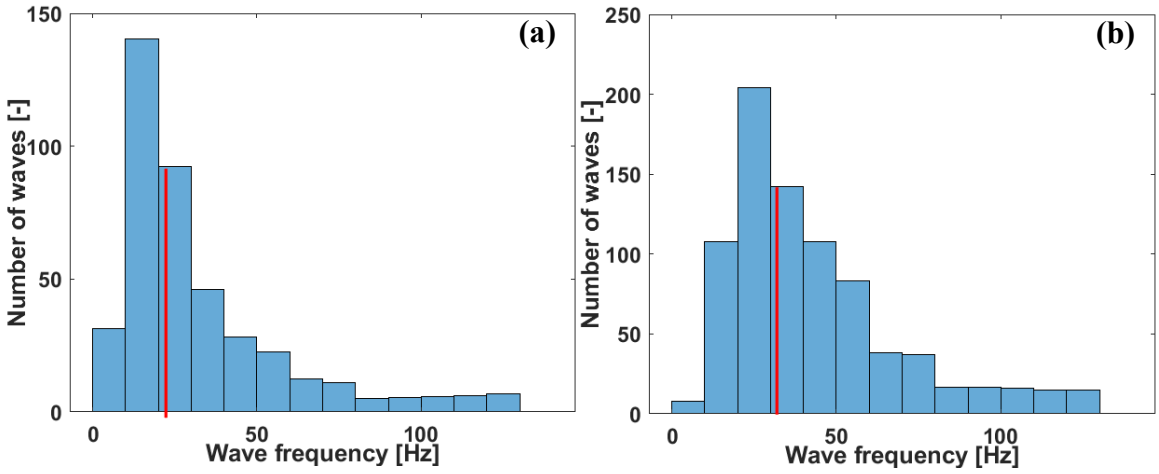

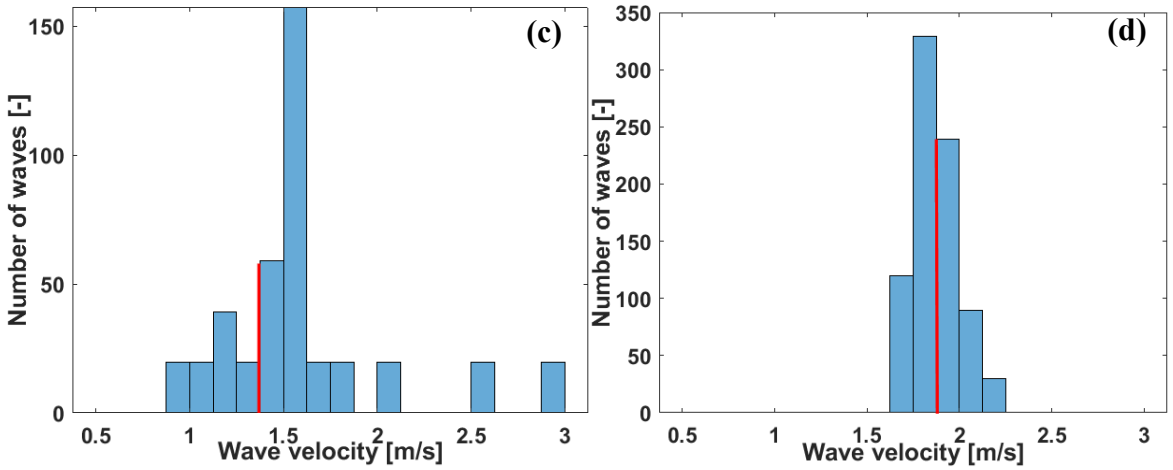

Figure 20. PDF of a. wave frequency for $G = 100\ kg/m^2s, x = 0.35, q = 1.5\ W/cm^2, n = 413$, b. wave frequency for $G = 200\ kg/m^2s, x = 0.34, q = 1.5\ W/cm^2, n = 807$, c. wave velocity for $G = 100\ kg/m^2s, x = 0.35, q = 1.5\ W/cm^2, n = 413$, d. wave velocity for $G = 200\ kg/m^2s, x = 0.34, q = 1.5\ W/cm^2, n = 807$. n is the total number of roll waves analyzed, red line is the mean value.

Fig. 21 shows a comparison between the mean wave velocity, liquid velocity and vapor velocity at constant heat flux in both upward and downward flows. The mean wave velocity, liquid velocity and vapor velocity all increased with vapor quality and vapor Reynolds number. In both flow configurations, the mean wave velocity was intermediate between the mean liquid and vapor velocities and was closer to the former. The difference between the mean wave velocity and mean liquid velocity $(U_w - U_l)$ decreased with mass flux. $U_w - U_l$ increased with vapor quality, but becomes independent of vapor quality at high vapor Reynolds number.

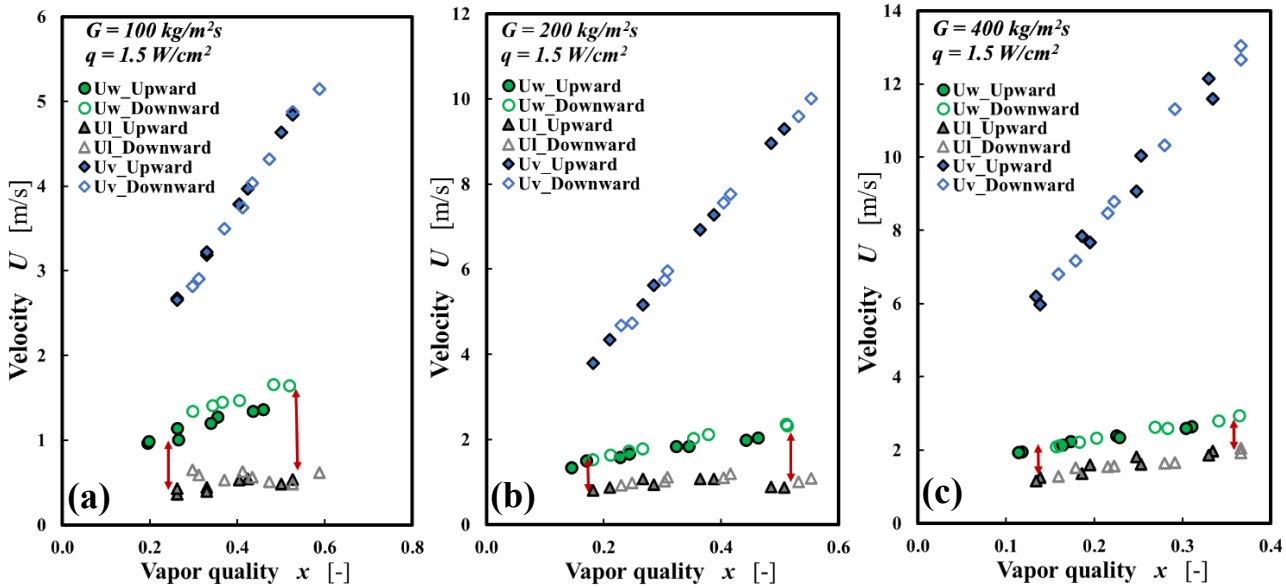

Figure 21. Comparison between mean wave velocity, liquid velocity and vapor velocity at constant heat flux for a. $G = 100\ kg/m^2s$, b. $G = 200\ kg/m^2s$ and c. $G = 400\ kg/m^2s$.

Figs. 22 and 23 show the evolution of the wave velocity and wave frequency versus the vapor quality in upward and downward flows for $100 \leq G \leq 400\ kg/m^2s$. At a given heat flux, both wave velocity and wave frequency increased with mass flux in both flow configurations. This is consistent with previous reports (Dasgupta et al., 2017; Kumar et al., 2002; Omebere-Iyari and Azzopardi, 2007). Wave velocity was generally higher in downward flow relative to upward flow for $Re_v \leq 30000\ kg/m^2s$ ($G \leq 200\ kg/m^2s$) but become similar in both configurations at $Re_v > 30000\ kg/m^2s$ ($G = 400\ kg/m^2s$) (Fig. 22). Gravity enhances the wave velocity in downward flow and has an opposite effect in upward flow. Conversely, at given mass flux and vapor quality, wave frequency was generally higher in upward flow relative to downward flow (Fig. 23). This is coherent with the lower interfacial shear stress measured in downward flow which in turn results in fewer roll wave formation. The difference between the mean wave frequency in upward and downward flows decreased with quality and mass flux. At lower mass flux, increase in heat flux resulted in more wave formation (particularly capillary waves) in downward flow and consequently higher wave frequency in downward flow than in upward flow (Fig. 23b).

Pearce (1979) proposed a correlation for the wave velocity for adiabatic two-phase upward flow (Eq. 35). The constant C in Eq. 36 was determined to be in the range of $0.51 \leq C \leq 0.61$ for tube diameters between $5\ mm \leq C \leq 10\ mm$ by Omebere-Iyari and Azzopardiet al., (2007). Following the approach of Omebere-Iyari and Azzopardiet al., (2007), the value of the constant for the $6\ mm$ diameter tube used for the current work is ≈ 0.53. In the current work, liquid entrainment (e) and its contribution to the calculation of the various hydrodynamic parameters was generally small across all flow configurations (see Fig. 24d). Therefore, computation of the mean liquid velocity ($\bar{u}_{lf}$) was done using Eq. 37. Pearce (1979)'s correlation reproduced the trend and provided a good estimation of the wave velocity at higher heat flux and higher mass flux (Fig. 22b-c). Similar prediction was obtained for downward flows.

$$U_w = \frac{C\bar{u}_{lf} + j_v\sqrt{\frac{\rho_v}{\rho_l}}}{C + \sqrt{\frac{\rho_v}{\rho_l}}} \tag{36}$$

$$\bar{u}_{lf} = \frac{G(1-x)}{\rho_l(1-\alpha)} \tag{37}$$

Sekoguchi et al., (1985) proposed a correlation for predicting the frequency of disturbance waves in upward flow as a function of the EÖtvos number (Eo), Reynolds number of the liquid (Re_l) and Froude number of the vapor (Fr_v) (Eq. 38). The correlation predicted the measured mean wave frequency in upward flow for $100 \leq G \leq 400\ kg/m^2s$ within $\pm 50\%$ and the measured mean wave frequency in upward flow for $G = 400\ kg/m^2s$ within $\pm 30\%$ (Figure 23c). Similar prediction was obtained for downward flow.

$$F_w = f_1 g_1 j_v D \tag{38}$$

where, $f_1 = 0.5 g_1 Eo^{-0.5} \ln Eo$, $g_1 = 0.0076 \ln \varphi - 0.51$, $Eo = \frac{gD^2(\rho_l - \rho_v)}{\sigma}$, $\varphi = \frac{Re_l^{2.5}}{Fr_v}$, $Fr_v = \frac{j_v}{\sqrt{gD}}$

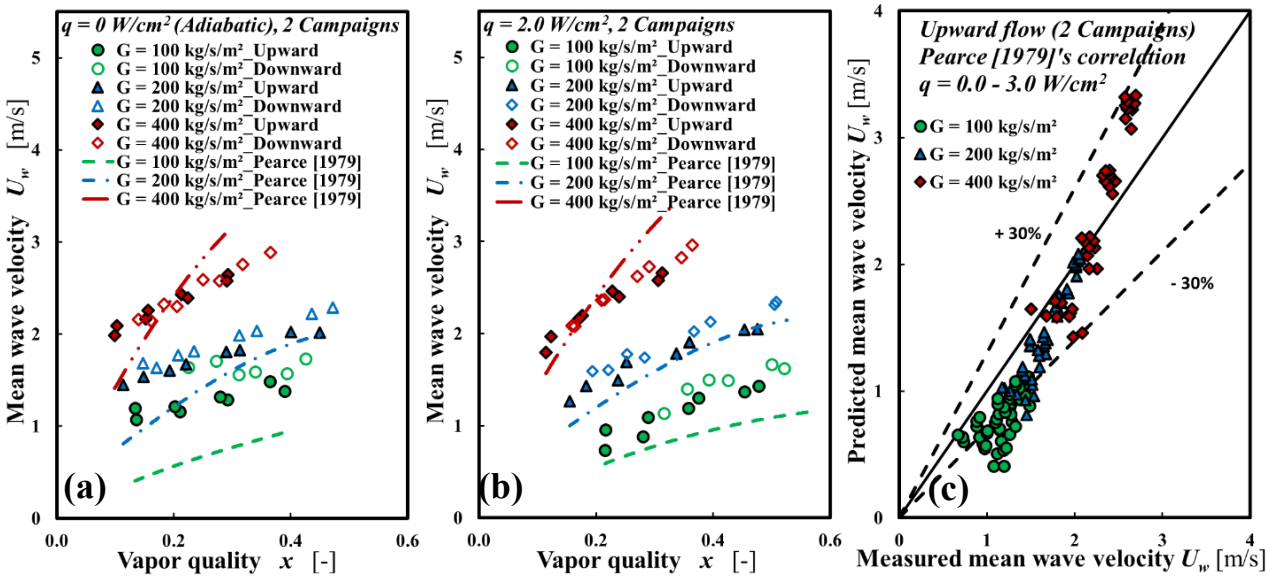

Figure 22. Mean wave velocity versus vapor quality in upward and downward flow. a. adiabatic flow, b. non-adiabatic flow, c. predicted mean wave velocity versus measured mean wave velocity.

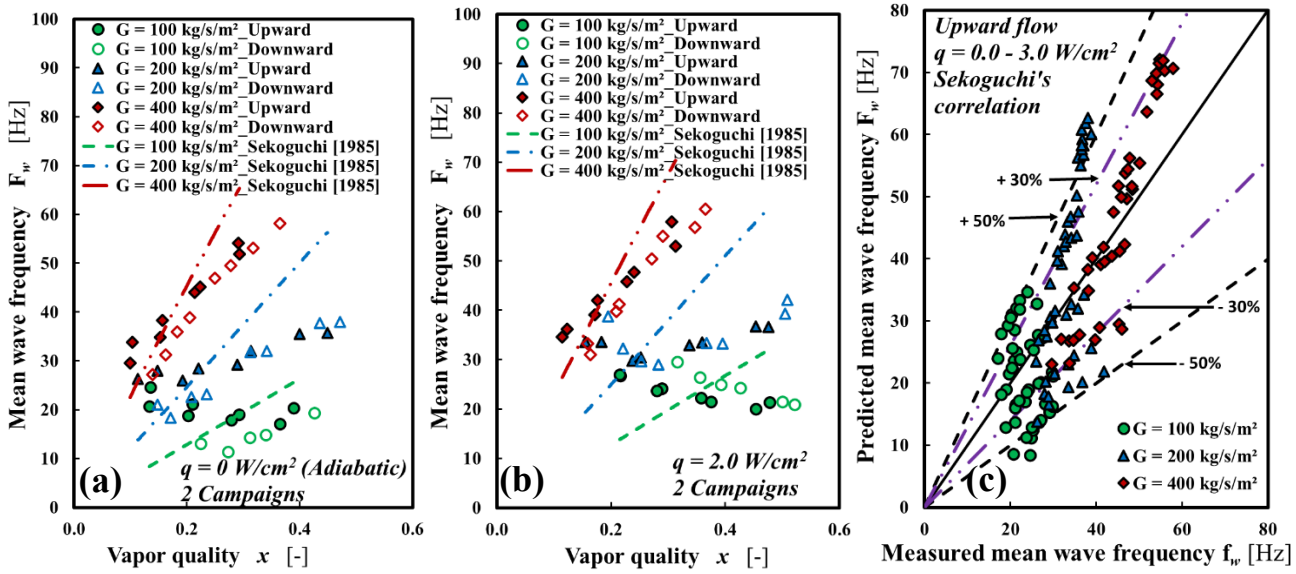

Figure 23. Mean wave frequency versus vapor quality in upward and downward flow. a. adiabatic flow, b. non-adiabatic flow, c. predicted mean wave frequency versus measured mean wave frequency.

The mean wave velocity and mean wave frequency showed significant dependence on wall heat flux in both flow configurations (Figs. 24 and 25). At lower vapor quality and lower mass flux, increase in wall heat flux resulted in decrease in wave velocity (Figs. 24a and 25a) and increase in wave frequency (Figs. 24b and 25b). These trends were more obvious in upward flow. Similar to mean wave frequency, the interfacial shear stress increased with wall heat flux, but at a much smaller scale

(Figs. 24d and 25d). The product of mean wave velocity and mean wave frequency (Figs. 24c and 25c) also increased with wall heat flux and at a scale similar to the interfacial shear stress. It appears that effect of wall heat flux on interfacial shear stress is well captured by the product of the wave velocity and wave frequency. The results suggest that correlations for predicting interfacial shear stress in boiling flow should capture the effect of these two wave parameters (particularly in flow conditions where the effect of heat flux on the interfacial shear stress is important).

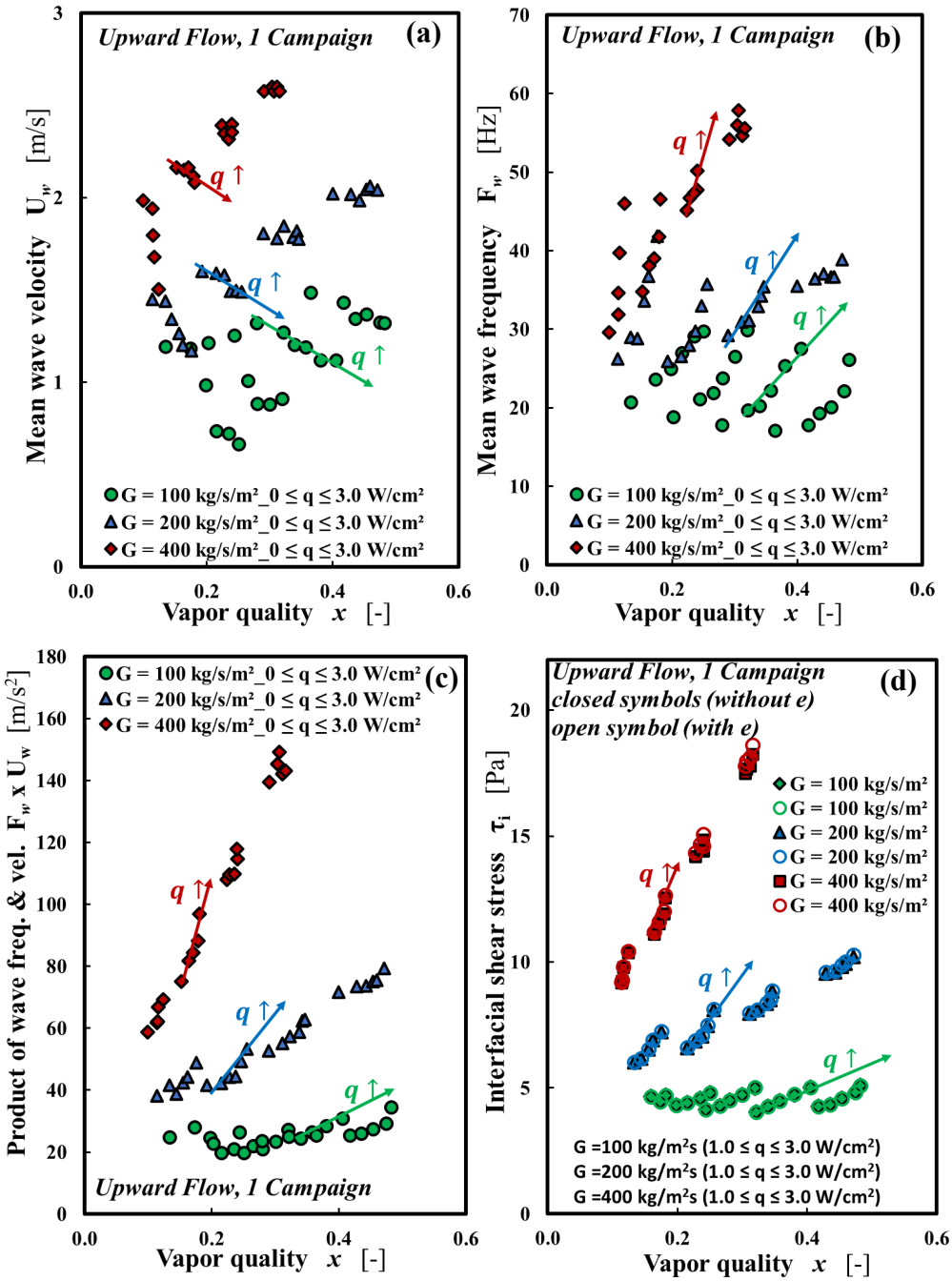

Figure 24. a. Mean wave velocity, b. mean wave frequency, c. product of mean wave velocity and mean wave frequency, d. interfacial shear stress versus vapor quality in upward flow.

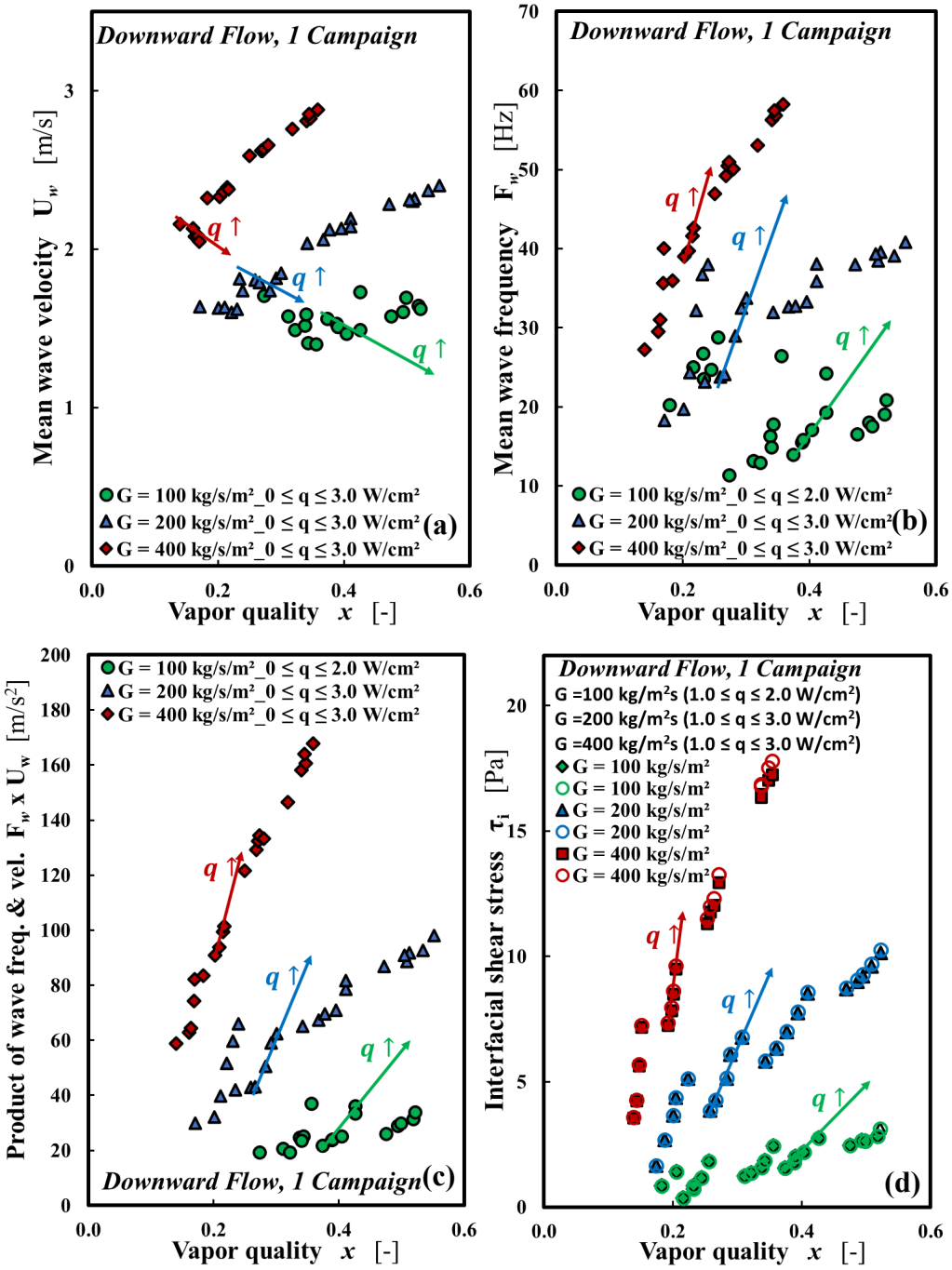

Figure 25. a. Mean wave velocity, b. mean wave frequency, c. product of mean wave velocity and mean wave frequency, d. interfacial shear stress versus vapor quality in downward flow.

Due to the coupling between τ_i and $F_w \times U_w$, a dimensionless parameter, $\tau_i/[F_w U_w(\rho_l - \rho_v)\delta]$ was plotted against the vapor quality (Fig. 26a-b). In upward flow, data for all the mass fluxes and heat fluxes collapsed within $\pm 10\%$ of a single curve (Fig. 26a). Similarly, in downward flow, data for all the mass fluxes and heat fluxes collapsed within $\pm 15\%$ of a single curve (Fig. 26b). It should be remarked that the slight deviation in the profile for $G = 100\ kg/m^2 s$ in downward flow was due to lower accuracy in $F_w \times U_w$ and difficulty in distinguishing between falling film and annular flow

regimes at lower flow rates. The lower accuracy in F_w and U_w at $G = 100\ kg/m^2s$ was due to the presence of significant number of ripples which made it difficult to analyze the roll waves independently. From the straight line fit in Figs. 26a and 26b, a correlation for predicting interfacial friction factor ratio in boiling flows is proposed (Eq. 39).

$$\frac{f_i}{f_v} = \frac{1}{f_v}\frac{2\tau_i}{\rho_v(U_v - U_l)^2} = \frac{1}{f_v}\frac{2F_w U_w(\rho_l - \rho_v)\delta(Ax+B)}{\rho_v(U_v - U_l)^2} \tag{39}$$

$$A \text{ and } B \approx \begin{cases} 1.9 \text{ and } 0.14 \text{ in upward flow} \\ 1.4 \text{ and } 0 \text{ in downward flow} \end{cases}, \quad 0 < q < 3\,W/cm^2,\ D = 6mm$$

Where A and B are constants, u_v is the vapor velocity, u_l is the liquid velocity and x is the vapor quality.

Figs. 26c and 26d provide comparisons between experimental interfacial friction factor ratio and that predicted by Eq. 39 for upward and downward flows respectively. For upward flow, the model predicted over 90% of the data within $\pm 20\%$, while for downward flow, the model predicted over 70% of the data within $\pm 20\%$. It should be remarked that while the values of B in Eq. 39 is expected to apply to other pipe diameters, the constant A may depend on pipe diameter. To use Eq. 39 for the prediction interfacial friction factor ratio, correlations for predicting F_w and U_w are required. The correlation of Pearce (1979) provided a reasonable prediction of U_w, particularly at higher mass flux, however, a correlation for predicting F_w is still required.

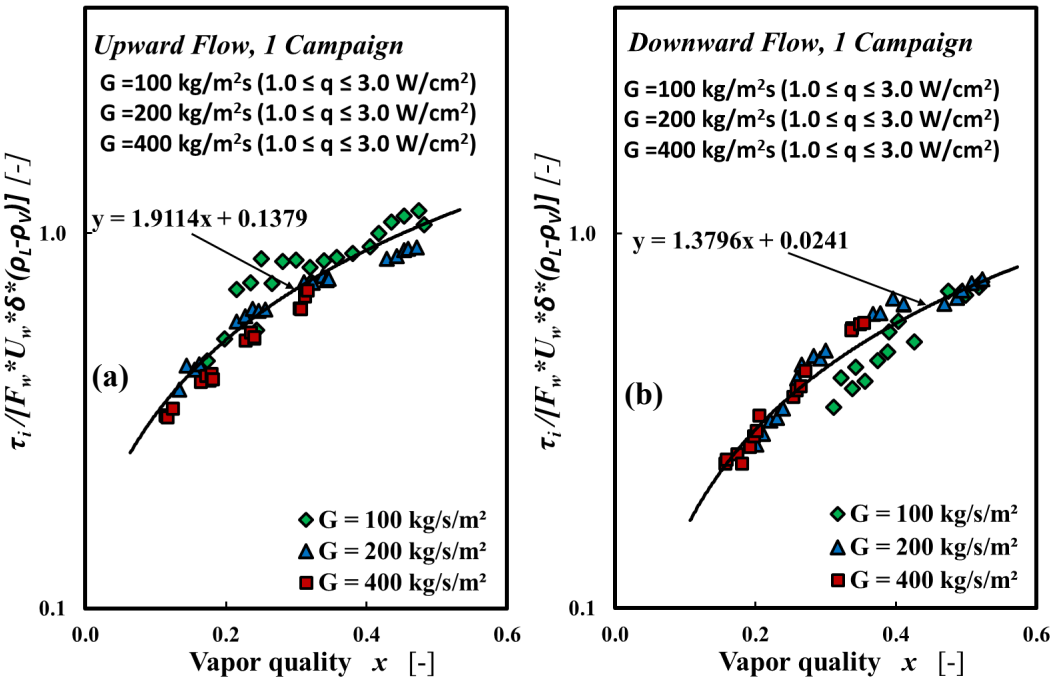

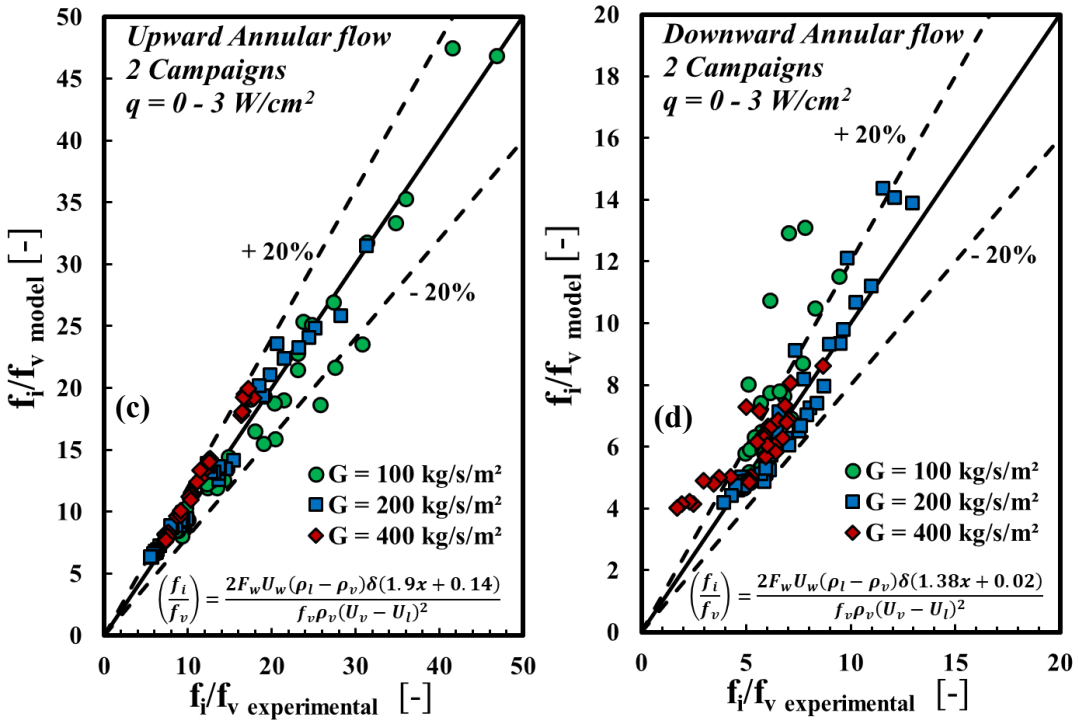

Figure 26. Dimensionless parameter versus quality for a. upward flow, b. downward flow. Predicted interfacial friction factor ratio versus experimental interfacial friction factor ratio for c. upward flow, d. downward flow.

Conclusions

This study presents a complete dataset on vertical flow boiling in tube in upward and downward configurations, including void fraction, wall and interfacial shear stresses, wall heat transfer and interfacial waves characteristics in annular flow. Most of the data are compared to models and correlations of the literature and improvement of some models is proposed. The main findings of the study are the following:

1. Bubble characteristics, void fraction (& vapor velocity), wall shear stress and heat transfer coefficient showed significant sensitivity to flow direction. The aforementioned parameters were generally higher in downward flow relative to upward flow for $G < 400\, kg/m^2 s$ and $x \leq 0.25$.

2. The void fraction is well predicted in upward flow by the drift flux model of Rouhani and Axelsson (1970) in intermittent flow and by the model of Zuber et al. (1967) in annular flows. In downward flow the model of the Rouhani and Axelsson (1970) is in good agreement with the data in intermittent, falling film and annular flow regimes. From the void fraction values, the averaged film thickness can be estimated in annular flows using Eq. 16, since the effect of the droplet entrainment rate estimated by Cioncolini et al. (2009) is negligible.

3. There was a strong coupling between wall shear stress and Heat Transfer Coefficient in both upward and downward flows. Wall shear stress was generally higher in boiling flow relative to adiabatic vapor-liquid two-phase flow because of the effect of bubble nucleation at the wall. The influence of wall heating on wall shear stress and heat transfer coefficient was more pronounced in downward flow relative to upward flow. Slight modifications of the correlation of Kim and Mudawar (2012) for the wall shear stress and of the correlation of Kim and Mudawar (2013a) for the Heat Transfer Coefficient are proposed for upward flow and extended to downward flows.

4. The Interfacial shear stress increases with the mass flux, quality and wall heat flux in upward and downward flows. The effect of the heat flux is more pronounced in downward flow. In upward flow the interfacial friction factor depends on both the film thickness and the Reynolds number of the vapor core and is well predicted by Eq. 35. The interfacial shear stress is strongly related to the structure of the interfacial waves (velocity and frequency). Wave velocities and frequencies have been determined by image processing. The wave frequency increased while the wave velocity decreased with the wall heat flux. The interfacial friction factor is found to depend on the product of the wave velocity and wave frequency. Eq. 39 provides a good prediction of the friction factor subject to a good prediction of the wave velocity and the wave frequency. The correlation of Pearce (1979) gives a reasonable estimation of the mean wave velocity, but some additional work is needed for a better prediction of the wave frequency to have a fully predictive model of the interfacial friction factor.

All the experimental data presented in this manuscript can be found in the supplementary material.

Acknowledgement

Petroleum Technology Development Fund (PTDF) is acknowledged for the PhD grant funding of P. Ayegba. The European Space Agency (ESA) and the French Space Agency (CNES) through the GDR MFA are acknowledged for the financial support in the building of the experimental set-up.

References

Al-Arabi, M., 1982. Turbulent heat transfer in the entrance region of a tube. Heat Transfer Engineering 3, 76–83.

Almabrok, A.A., Aliyu, A.M., Lao, L., Yeung, H., 2016. Gas/liquid flow behaviours in a downward section of large diameter vertical serpentine pipes. International Journal of Multiphase Flow 78, 25–43.

Asali, J.C., Hanratty, T.J., Andreussi, P., 1985. Interfacial drag and film height for vertical annular flow. AIChE Journal 31, 895–902.

Azzopardi, B.J., 1986. Disturbance wave frequencies, velocities and spacing in vertical annular two-phase flow. Nuclear Engineering and Design 92, 121–133.

Barbosa, J.R., Hewitt, G.F., Richardson, S.M., 2003. High-speed visualisation of nucleate boiling in vertical annular flow. International Journal of Heat and Mass Transfer 46, 5153–5160.

Belt, R.J., Van't Westende, J.M.C., Portela, L.M., 2009. Prediction of the interfacial shear-stress in vertical annular flow. International Journal of Multiphase Flow 35, 689–697.

Bhagwat, S.M., Ghajar, A.J., 2017. Experimental investigation of non-boiling gas-liquid two phase flow in downward inclined pipes. Experimental Thermal and Fluid Science 89, 219–237.

Bhagwat, S.M., Ghajar, A.J., 2015. An Empirical Model to Predict the Transition between Stratified and Nonstratified Gas-Liquid Two-Phase Flow in Horizontal and Downward Inclined Pipes. Heat Transfer Engineering 36, 1485–1494.

Bhagwat, S.M., Ghajar, A.J., 2014. A flow pattern independent drift flux model based void fraction correlation for a wide range of gas-liquid two phase flow. International Journal of Multiphase Flow 59, 186–205.

Bhagwat, S.M., Ghajar, A.J., 2012. Similarities and differences in the flow patterns and void fraction in vertical upward and downward two phase flow. Experimental Thermal and Fluid Science 39, 213–227.

Canière, H., T'joen, C., Willockx, A., de Paepe, M., Christians, M., van Rooyen, E., Liebenberg, L., Meyer, J.P., 2007. Horizontal two-phase flow characterization for small diameter tubes with a capacitance sensor. Measurement Science and Technology 18, 2898–2906.

Ceccio, S.L., George, D.L., 1996. A Review of Electrical Impedance Techniques for the Measurement of Multiphase Flows. Journal of Fluids Engineering 118, 391–399.

Celata, G.P., Zummo, G., 2009. Flow Boiling Heat Transfer in Microgravity: Recent Progress. Multiphase Science and Technology 21, 187–212.

Chen, L., Tian, Y.S., Karayiannis, T.G., 2006. The effect of tube diameter on vertical two-phase flow regimes in small tubes. International Journal of Heat and Mass Transfer 49, 4220–4230.

Cicchitti, A., Lombardi, C., Silvestri, M., Soldaini, G., Zavalluilli, R., 1960. Two-phase cooling experiments-pressure drop, heat transfer and burnout measurements. Energia Nucleare 7, 407–425.

Cioncolini, A., Thome, J.R., 2017. Pressure drop prediction in annular two-phase flow in macroscale tubes and channels. International Journal of Multiphase Flow 89, 321–330.

Cioncolini, A., Thome, J.R., 2012. Void fraction prediction in annular two-phase flow. International Journal of Multiphase Flow 43, 72–84.

Cioncolini, A., Thome, J.R., 2011. Algebraic turbulence modeling in adiabatic and evaporating annular two-phase flow. International Journal of Heat and Fluid Flow 32, 805–817.

Cioncolini, A., Thome, J.R., Lombardi, C., 2009. Unified macro-to-microscale method to predict two-phase frictional pressure drops of annular flows. International Journal of Multiphase Flow 35, 1138–1148.

Colin, C., Fabre, J., McQuillen, J., 1996. Bubble and slug flow at microgravity conditions: state of knowledge and open questions. Chemical Engineering Communications 141–142, 155–173.

Dalkilic, A.S., Laohalertdecha, S., Wongwises, S., 2008. Two-phase friction factor in vertical downward flow in high mass flux region of refrigerant HFC-134a during condensation. International Communications in Heat and Mass Transfer 35, 1147–1152.

Dasgupta, A., Chandraker, D.K., Kshirasagar, S., Reddy, B.R., Rajalakshmi, R., Nayak, A.K., Walker, S.P., Vijayan, P.K., Hewitt, G.F., 2017. Experimental investigation on dominant waves in upward air-water two-phase flow in churn and annular regime. Experimental Thermal and Fluid Science 81, 147–163.

Davis, E.J., Anderson, G.H., 1966. The incipience of nucleate boiling in forced convection flow. AIChE Journal 12, 774–780.

Dittus, E., Boelter, L., 1930. Experiments with fluid friction roughened pipes. Publication on Engineering 2, 443.

Enoki, K., Ono, M., Okawa, T., Kristiawan, B., Wijayanta, A.T., 2020. Water flow boiling heat transfer in vertical minichannel. Experimental Thermal and Fluid Science 117.

Fore, L.B., Beus, S.G., Bauer, R.C., 2000. Interfacial friction in gas-liquid annular flow: Analogies to full and transition roughness. International Journal of Multiphase Flow 26, 1755–1769.

Friedel, L., 1979. Improved friction pressure drop correlations for horizontal and vertical two-phase pipe flow, in: European Two-Phase Flow Meeting.

Fukano, T., Furukawa, T., 1998. Prediction of The Effects of Liquid Viscosity on Interfacial Shear Stress and Frictional Pressure Drop in Vertical Upward Gas-Liquid Annular Flow. International Journal of Multiphase Flow 24, 587–603.

Gardenghi, Á.R., Filho, E. dos S., Chagas, D.G., Scagnolatto, G., Oliveira, R.M., Tibiriçá, C.B., 2020. Overview of Void Fraction Measurement Techniques, Databases and Correlations for Two-Phase Flow in Small Diameter Channels. Fluids 5, 216.

Gnielinski, V., 1976. New equations for heat and mass transfer in turbulent pipe and channel flow. International Journal of Chemical Engineering 16, 359–368.

Gomyo, T., Asano, H., 2016. Void Fraction Characteristics of One-Component Gas-Liquid Two-Phase Flow in Small Diameter Tubes. Interfacial Phenomena and Heat Transfer 4, 1–18.

Ishii, M., 1977. One-dimensional drift-flux model and constitutive equations for relative motion between phases in various two-phase flow regimes, ANL-77-47.

Kandlikar, S.G., 1990. A general correlation for saturated two-phase flow boiling heat transfer inside horizontal and vertical tubes. Journal of Heat Transfer 112, 219–228.

Kew, P.A., Cornwell, K., 1997. Correlations for the prediction of boiling heat transfer in small-diameter channels. Applied Thermal Engineering 17, 705–715. https://doi.org/10.1016/s1359-4311(96)00071-3

Kharangate, C.R., O'Neill, L.E., Mudawar, I., 2016. Effects of two-phase inlet quality, mass velocity, flow orientation, and heating perimeter on flow boiling in a rectangular channel: Part 1 – Two-phase flow and heat transfer results. International Journal of Heat and Mass Transfer 103, 1261–1279.

Khodabandeh, R., 2005. Pressure drop in riser and evaporator in an advanced two-phase thermosyphon loop. International Journal of Refrigeration 28, 725–734.

Kim, S., Mudawar, I., 2014. Review of databases and predictive methods for pressure drop in adiabatic, condensing and boiling mini/micro-channel flows. International Journal of Heat and Mass Transfer 77, 74–97.

Kim, S.M., Mudawar, I., 2013a. Universal approach to predicting saturated flow boiling heat transfer in mini/micro-channels – Part II. Two-phase heat transfer coefficient. International Journal of Heat and Mass Transfer 64, 1239–1256.

Kim, S.M., Mudawar, I., 2013b. Universal approach to predicting two-phase frictional pressure drop for mini/micro-channel saturated flow boiling. International Journal of Heat and Mass Transfer 58, 718–734.

Kim, S.M., Mudawar, I., 2012. Universal approach to predicting two-phase frictional pressure drop for adiabatic and condensing mini/micro-channel flows. International Journal of Heat and Mass Transfer 55, 3246–3261.

Kocamustafaogullari, G., Ishii, M., 1983. Aire interfaciale et densité de sites de nucléation dans les systèmes en ébullition. International Journal of Heat and Mass Transfer 26, 1377–1387.

Konishi, C., Mudawar, I., 2015. Review of flow boiling and critical heat flux in microgravity. International Journal of Heat and Mass Transfer 80, 469–493.

Kumar, R., Gottmann, M., Sridhar, K.R., 2002. Film thickness and wave velocity measurements in a vertical duct. Journal of Fluids Engineering, Transactions of the ASME 124, 634–642.

Layssac, T., 2018. Contribution à l'étude phénoménologique de l'ébullition convective en mini-canal. Université de Lyon.

Liu, Z., Winterton, R.H.S., 1991. A general correlation for saturated and subcooled flow boiling in tubes and annuli, based on a nucleate pool boiling equation. International Journal of Heat and Mass Transfer 34, 2759–2766.

Lockhart, R.W., Martinelli, R.C., 1949. Proposed correlation of data for isothermal two-phase, two-component flow in pipes. Chem. Eng. Prog. 45, 39–48.

Lopes, J.C., Dukler, A.E., 1986. Droplet entrainment in vertical annular flow and its contribution to momentum transfer. AIChE Journal 32, 1500–1515.

Maqbool, M.H., Palm, B., Khodabandeh, R., 2012. Flow boiling of ammonia in vertical small diameter tubes: Two phase frictional pressure drop results and assessment of prediction methods. International Journal of Thermal Sciences 54, 1–12.

Martin, S.C., 1976. Vertically downward two-phase slug flow. Journal of Fluids Engineering, Transactions of the ASME 98, 715–722.

Mishima, K., Ishii, M., 1984. Flow regime transition criteria for upward two-phase flow in vertical tubes. International Journal of Heat and Mass Transfer 27, 723–737.

Muller-Steinhagen, H., Heck, K., 1986. Flow boiling in tube under normal gravity and microgravity conditions. Chemical Engineering and Processing: Process Intensification 20, 297–308.

Narcy, M., de Malmazet, E., Colin, C., 2014. Flow boiling in tube under normal gravity and microgravity conditions. International Journal of Multiphase Flow 60, 50–63.

Omebere-Iyari, N. K. Azzopardi, B.J., 2007. A study of flow patterns for gas/liquid flow in small diameter tubes. Chemical Engineering Research and Design 85, 180–192.

Pearce, D.L., 1979. Film waves in horizontal annular flow: space time correlator experiments, Central Electricity Research Laboratories.

Rouhani, S.Z., Axelsson, E., 1970. Calculation of void volume fraction in the subcooled and quality boiling regions. International Journal of Heat and Mass Transfer 13, 383–393.

Sekoguchi, K., Takashi, U., Osamu, T., 1985. An investigation of the flow characteristics in the disturbance wave region of annular flow: 2nd report, on correlation of principal flow parameters. Trans. Jpn. Soc. Mech. Eng. 51, 1798–1806.

Shang Ying-Qi, Qi Hong, Ma Yun Long, Wu Ya Lin, Zhang Yan, Chen Jing, 2017. Study on sapphire microstructure processing technology based on wet etching. International Journal of Modern Physics B 31.

Taitel, Y., Bornea, D., Dukler, A.E., 1980. Modelling flow pattern transitions for steady upward gas-liquid flow in vertical tubes. AIChE Journal 26, 345–354.

Tran, C.C., Gupta, S., Newell, T.A., Chato, J.C., Phoenix, H., 2000. A Study of Refrigerant Void Fraction and Pressure Drop in Return Bends and Development of a New Two-Phase Experimental Apparatus General Motors Corporation 61801.

Usui, K., 1989. Vertically downward two-phase flow, (II): Flow regime transition criteria. Journal of Nuclear Science and Technology 26, 1013–1022.

Usui, K., Sato, K., 1989. Vertically downward two-phase flow, (I) void distribution and average void fraction. Journal of Nuclear Science and Technology 26, 670–680.

Wallis, G., 1969. One dimensional two-phase flow. McGraw-Hill.

Wang, M., Mei, Y., Li, X., Burgos, R., Boroyevich, D., Lu, G.Q., 2018. How to determine surface roughness of copper substrate for robust pressureless sintered silver in air. Materials Letters 228, 327–330.

Woldesemayat, M.A., Ghajar, A.J., 2007. Comparison of void fraction correlations for different flow patterns in horizontal and upward inclined pipes. International Journal of Multiphase Flow 33, 347–370.

Wu, B., Firouzi, M., Mitchell, T., Rufford, T.E., Leonardi, C., Towler, B., 2017. A critical review of flow maps for gas-liquid flows in vertical pipes and annuli. Chemical Engineering Journal.

Zuber, N., Staub, F.W., Bijwaard, G., Kroeger, P.G., 1967. Steady State and Transient Void Fraction in Two-Phase Flow Systems. General Electric Co. Report GEAP-5417.

Appendix

The uncertainties in the measured parameters are presented in this section followed by results of single-phase flow validation.

Measurement uncertainties

Uncertainties in measured inlet and outlet vapor qualities are determined by Eq. A1 and Eq. A4. Table A1 provides a summary of uncertainties and low and high vapor qualities.

$$\delta x_{in} = \left\{ \left[\frac{4\delta P_{ph}}{G\pi D^2 h_{lv}} \right]^2 + \left[\frac{-4P_{ph}\delta G}{G^2\pi D^2 h_{lv}} \right]^2 + \left[\frac{-8P_{ph}\delta D}{G\pi D^3 h_{lv}} \right]^2 + \left[\frac{-Cp_l \delta T}{h_{lv}} \right]^2 \right\}^{0.5} \quad \text{A1}$$

$$\delta G = \sqrt{\left(\frac{4}{\pi D^2} \delta \dot{m} \right)^2 + \left(\frac{-8\dot{m}}{\pi D^3} \delta D \right)^2}, \qquad \delta \dot{m} = 0.5\% \times \dot{m} \quad \text{A2}$$

$$\delta P_{ph} = \sqrt{(U_{rms}\delta I_{rms})^2 + (I_{rms}\delta U_{rms})^2} \quad \text{A3}$$

$\delta I_{rms} = \pm 10\ mA$, $\delta U_{rms} = \pm 45\ mV$

$$\delta x_{out} = \delta x_{in} + \left\{ \left[\frac{4L\delta q_{eff}}{GD\left[h_{lv} + Cp_l\left(T_{sat,meas} - T_z\right)\right]} \right]^2 + \left[\frac{4q_{eff}\delta L}{GD\left[h_{lv} + Cp_l\left(T_{sat,meas} - T_z\right)\right]} \right]^2 + \left[\frac{-4Lq_{eff}\delta G}{G^2 D\left[h_{lv} + Cp_l\left(T_{sat,meas} - T_z\right)\right]} \right]^2 + \left[\frac{-8Lq_{eff}\delta D}{GD^2\left[h_{lv} + Cp_l\left(T_{sat,meas} - T_z\right)\right]} \right]^2 + \left[\frac{-Cp_l\delta T}{h_{lv} + Cp_l\left(T_{sat,meas} - T_z\right)} \right]^2 \right\}^{0.5} \quad \text{A4}$$

$$q_{eff} = \sqrt{\left(\frac{\delta P_{ITO}}{\pi DL} \right)^2 + \left(\frac{-P_{ITO}\delta D}{\pi D^2 L} \right)^2 + \left(\frac{-P_{ITO}\delta L}{\pi DL^2} \right)^2} \quad \text{A5}$$

$$\delta P_{ITO} = \sqrt{(U_{ITO}\delta I_{ITO})^2 + (I_{ITO}\delta U_{ITO})^2} \quad \text{A6}$$

$\delta I_{ITO} = \pm 10\ mA$, $\delta U_{ITO} = \pm 30\ mV$

Table A1: Uncertainty in calculated interfacial shear stress (Pa).

	low x		high x	
	$x(-)$	$\delta x(-)$	$x(-)$	$\delta x(-)$
inlet	0.1090	0.0099(9.08%)	0.2853	0.2770(4.73%)
outlet	0.1615	0.0129(7.99%)	0.4211	0.0181(4.29%)

Assuming negligible error from computed liquid entrainment, the uncertainty in the measured liquid film thickness is given by;

$$\delta(\delta) = \left[\left(\frac{\delta D}{2}\left(1-\sqrt{\alpha}\right)\right)^2 + \left(\frac{D}{2}\left(\frac{-\delta\alpha}{2\sqrt{\alpha}}\right)\right)^2\right]^{0.5} \quad (\ \delta\alpha \approx \alpha \times 6/100) \qquad \text{A7}$$

The mean estimated errors for low to high vapor qualities corresponding to high and low liquid film thickness is shown in Table A2. Errors in measured film thickness of up to 70% can be obtained for very high vapor qualities corresponding to very thin liquid film.

Table A2: Error estimation for calculated liquid film thickness

	$\mathbf{0.10 < x < 0.20}$	$\mathbf{0.20 < x < 0.35}$	$\boldsymbol{x > 0.35}$
$\boldsymbol{\delta(\delta)/_{\delta} \times 100}$	3%	15%	45%

The uncertainty of the measured heat transfer coefficient was determined by;

$$\delta h_i = \left[\left(\frac{\delta q_{eff}(T_{ow}-T_{i\infty})}{T_{ow}-T_{i\infty}-ln\left(\frac{R_o}{R_i}\right)\frac{R_o}{k}q_{eff}}\right)^2 + \left(\frac{-q_{eff}\delta T_{ow}}{\left(T_{ow}-T_{i\infty}-ln\left(\frac{R_o}{R_i}\right)\frac{R_o}{k}q_{eff}\right)^2}\right)^2 + \left(\frac{q_{eff}\delta T_{i\infty}}{\left(T_{ow}-T_{i\infty}-ln\left(\frac{R_o}{R_i}\right)\frac{R_o}{k}q_{eff}\right)^2}\right)^2\right]^{0.5} \qquad \text{A8}$$

Table A3: Uncertainty in calculated heat transfer coefficient (W/m^2K)

	$\boldsymbol{q = 1.0\,W/cm^2\ (T_{ow} - T_{i\infty} = 5^oC)}$	$\boldsymbol{q = 3.0\,W/cm^2\ (T_{ow} - T_{i\infty} = 18^oC)}$
$\boldsymbol{\delta h_i\ (W/m^2K)}$	229.5	114.5

$$\tau_w = \left[\left(\delta\Delta P_f D/(4L)\right)^2 + \left(\Delta P_f \delta D/(4L)\right)^2 + \left(-\Delta P_f D\delta L/(4L^2)\right)^2\right]^{0.5} \quad \text{A9}$$

Neglecting the acceleration term ($\Delta P_f = \Delta P - [\rho_l(1-\alpha) + \rho_v\alpha]gL$); the uncertainty in the measured frictional pressure drop ($\delta\Delta P_f$) is given by;

$$\Delta P_f = \sqrt{(\delta\Delta P)^2 + (-\delta L[\rho_l(1-\alpha) + \rho_v\alpha]g)^2 + ([\rho_l - \rho_v]gL\delta\alpha)^2} \quad \text{A10}$$

$\delta\Delta P = \pm 0.27\ mbar$

Table A4: Uncertainty in calculated wall shear stress (%).

$\boldsymbol{\tau_w(Pa)}$	$\boldsymbol{\alpha = 0.3}$	$\boldsymbol{\alpha = 0.7}$	$\boldsymbol{\alpha = 0.9}$
$\mathbf{3.13}$	$15.4 \pm 0.5\%$	$29.1 \pm 0.5\%$	$36.6 \pm 0.5\%$
$\mathbf{9.38}$	$9.5 \pm 0.5\%$	$12.5 \pm 0.5\%$	$14.5 \pm 0.5\%$
$\mathbf{15.63}$	$8.7 \pm 0.5\%$	$10.0 \pm 0.5\%$	$11.0 \pm 0.5\%$

$$\delta\tau_i = \left[\left(\frac{D\sqrt{\alpha}}{4L}\delta(\Delta P)\right)^2 + \left(\left(\frac{\Delta P\sqrt{\alpha}}{4L} + \frac{\rho_v g\sqrt{\alpha}}{4}\right)\delta(D)\right)^2 + \left(\frac{-\Delta PD\sqrt{\alpha}}{4L^2}\delta(L)\right)^2 + \left(\left(\frac{-\Delta PD}{8L} + \frac{\rho_v gD}{8}\right)\frac{\delta(\alpha)}{\sqrt{\alpha}}\right)^2\right]^{0.5} \quad \text{A11}$$

Table A5: Uncertainty in calculated interfacial shear stress (Pa).

	$\boldsymbol{\alpha = 0.30}$	$\boldsymbol{\alpha = 0.70}$	$\boldsymbol{\alpha = 0.90}$
$\boldsymbol{\delta\tau_i\ (Pa)}$	0.196	0.303	0.346

Single-phase flow validation

Fig. A1 shows results of single-phase flow validation for wall friction factor and heat transfer coefficient.

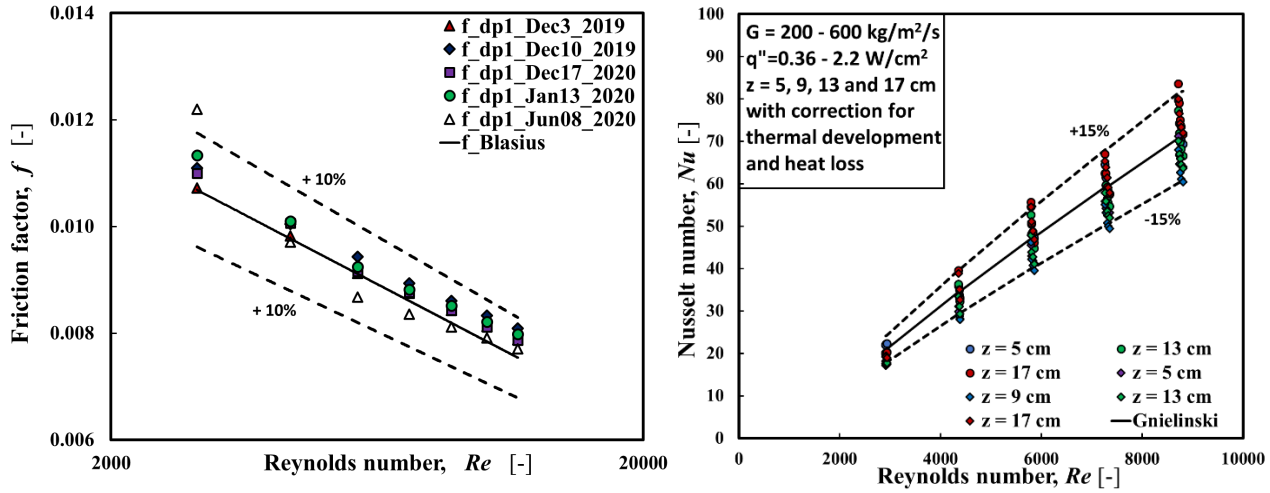

Figure A1. Single-phase validation for wall friction factor (left) and heat transfer (right).

Comparison between wall shear stress in upward and downward non-boiling flows

Fig. A2 shows plots of wall shear stress versus quality in upward and downward flows.

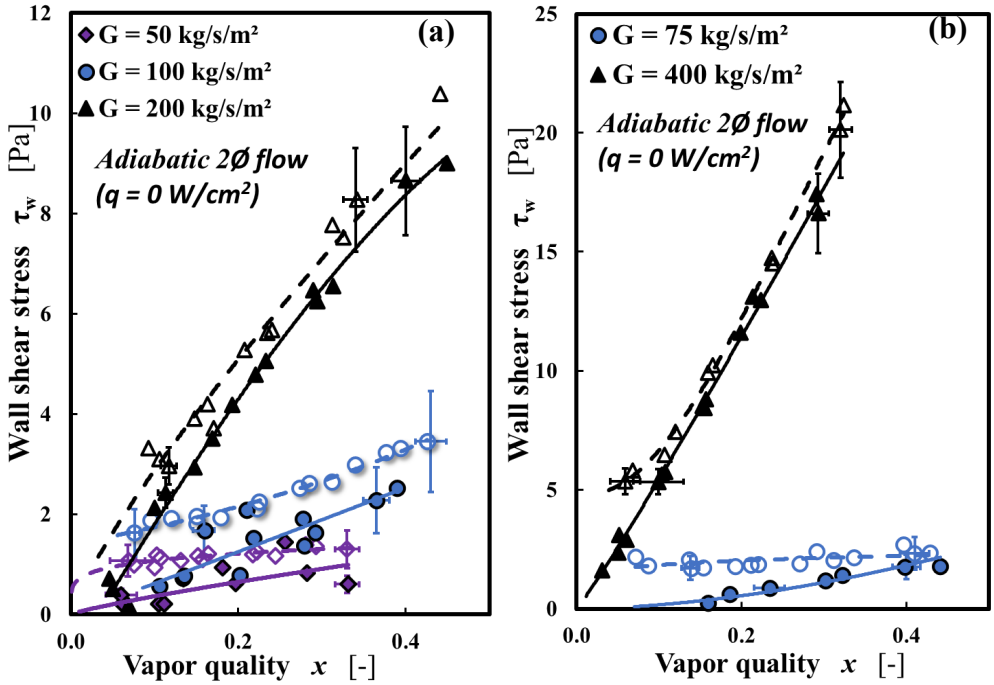

Fig. A2. Comparison of measured wall shear stress in upward and downward flow; upward flow (closed symbol), downward flow (open symbols). The lines are polynomial fits that provide trends; upward flow (solid lines), downward flow (dashed lines).